Quarterly Journal of the Royal Meteorological Society Q. J. R. Meteorol. Soc. (2016) DOI:10.1002/qj.2684

Clear-sky stable boundary layers with low winds over snow-covered surfaces. Part 2: Process sensitivity

H. A. M. Sterk,[a]* G. J. Steeneveld,[a] F. C. Bosveld,[b] T. Vihma,[c]
P. S. Anderson[d] and A. A. M. Holtslag[a]

[a] *Meteorology and Air Quality Section, Wageningen University, The Netherlands*
[b] *Royal Netherlands Meteorological Institute, De Bilt, The Netherlands*
[c] *Finnish Meteorological Institute, Helsinki, Finland*
[d] *Scottish Association for Marine Science, Oban, UK*

*Correspondence to: H. A. M. Sterk, Meteorology and Air Quality Section, Wageningen University, PO Box 47, 6700 AA Wageningen, the Netherlands. E-mail: sterk.ham@gmail.com

This study evaluates the relative impact of snow-surface coupling, long-wave radiation, and turbulent mixing on the development of the stable boundary layer over snow. Observations at three sites are compared to WRF single-column model (SCM) simulations. All three sites have snow-covered surfaces but are otherwise contrasting: Cabauw (Netherlands, grass), Sodankylä (Finland, needle-leaf forest) and Halley (Antarctica, ice shelf). All cases are characterized by stable, clear-sky, and calm conditions. Part 1 of this study determined the optimal SCM forcing strategy. In this study, the process intensities from that reference are perturbed to study their relative significance and to assess which process could be responsible for the most optimal agreement between model and observation.

The analysis reveals a large variability in the modelled atmospheric state and surface parameters. Overall, the modelled gradients of temperature and moisture are underestimated but decreasing the process intensities improves this. The impact is strongest with reduced mixing, though this then causes the model to overestimate the near-surface wind speed.

To study the surface energy balance terms, we use so-called 'process diagrams'. The achieved variation between the sensitivity runs indicates the model sensitivity to each process. The overall sensitivity is similar for the three sites but the relative offsets in the position of the sensitivity runs with respect to the observations differ, hampering general recommendations for model improvement. Furthermore, sometimes a meaningful interpretation of observations is troublesome, which hampers the comparison with model results. Radiation is relatively more important at Cabauw and Sodankylä, whilst coupling plays a more important role at Halley.

The sensitivity analysis is performed with two boundary-layer schemes (MYJ, YSU). YSU generates larger, more accurate gradients of atmospheric temperature and humidity, while wind speeds are predicted better with MYJ. The behaviour of an increase in 2 m temperature with decreased mixing is most obvious with YSU.

Key Words: stable boundary layer; modelling; WRF; snow-surface; low wind speeds; surface coupling; long-wave radiation; turbulent mixing

Received 19 August 2014; Revised 13 August 2015; Accepted 28 September 2015; Published online in Wiley Online Library

1. Introduction

A single-column model (SCM) is a convenient tool to study the physical processes that are omnipresent in the boundary layer (BL; Baas *et al.*, 2010; Bosveld *et al.*, 2014) and can thus be used to improve our understanding of the stable boundary layer (SBL). SBL modelling is challenging due to a myriad of relatively small-scale processes that may act simultaneously, e.g. land-surface coupling, radiative effects, turbulent mixing, the presence of clouds or fog, subsidence, advection, gravity waves, and drainage and katabatic flows (Delage, 1997; Mahrt *et al.*, 1998; Mahrt, 1999, 2014; Steeneveld *et al.*, 2006; Williams *et al.*, 2013). Moreover, the physical processes and their interactions are perhaps not completely understood, and may furthermore be represented incompletely in models. Also, different SBL regimes can be distinguished, i.e. the flow can be continuously or intermittently turbulent, or even virtually absent (Van de Wiel *et al.*, 2002, 2012; Steeneveld *et al.*, 2006; Mahrt, 2014). This affects the SBL evolution and the vertical and horizontal exchanges (Holtslag *et al.*, 2006, 2013).

In the previous Part 1, 3D and SCM versions of the Weather Research and Forecasting model (WRF; Skamarock *et al.*, 2008) were presented for three similar but contrasting land surfaces. All three cases were over snow, and for stable, low wind speed and cloud-free conditions which are highly problematic for numerical atmospheric models (Edwards *et al.*, 2011; Atlaskin and Vihma, 2012; Holtslag *et al.*, 2013). The cases differed in surface type and location with the first case selected from the Cabauw dataset in the Netherlands (snow on grass/crop-land), the second case from the Sodankylä dataset in northern Finland (snow in a needle-leaf forest) and the third case from the Halley dataset in Antarctica (snow on an ice shelf). The selected cases were stably stratified with wind speeds below $5\,\mathrm{m\,s^{-1}}$ at the 10/8 m mast level, and relatively low wind speeds aloft. In all cases a so-called type I SBL was selected where, under very stable circumstances and low wind speeds, radiative cooling is very important and the shape of the potential temperature (θ) profile is approximately exponential, or concave up ($\partial^2\theta/\partial z^2 < 0$) (Van Ulden and Holtslag, 1985; Vogelezang and Holtslag, 1996) A more detailed description of the cases is given in Part 1 of this study (Sterk *et al.*, 2015).

The WRF-SCM needs to be driven by realistic forcings from the 3D atmosphere (Baas *et al.*, 2010). Part 1 studied the impact of forcing conditions on the model performance, where we distinguished between strategies that

(a) do not prescribe any lateral forcings,
(b) prescribe a varying geostrophic wind speed (U_g) in time,
(c) prescribe momentum advection on top of (b),
(d) prescribe θ and specific humidity (q) advection on top of (c), and
(e) force the SCM to the 3D field above a threshold height sufficiently above the BL.

Since observations of the forcings are in general not available at sufficiently high resolution in time and space, we rely on output from the WRF-3D runs.

Part 1 describes how the best SCM results were found with the set (d) forcings: varying U_g in time, and prescribing momentum, θ and q advection obtained by WRF-3D. Therefore the results corresponded to the WRF-3D results, and were in closer agreement with observations than when neglecting these advections. For all sites, the SCM underestimated the strengths of the θ and q inversions. With the Yonsei University (YSU) BL scheme, stronger θ inversions were found, which were closer in agreement with observations than with the Mellor–Yamada–Janjić (MYJ) BL scheme used previously. Unfortunately, the skill for wind speed and q then deteriorated such that better results were obtained with MYJ. Differences between the simulations with various long-wave radiation schemes were small.

Part 2 (presented here) continues these studies and performs a systematic sensitivity analysis using the WRF-SCM. We focus on snow-surface coupling, long-wave radiation and turbulent mixing as the key processes that define the SBL development and structure (André and Mahrt, 1982; Beljaars and Holtslag, 1991; Steeneveld *et al.*, 2006; Bosveld *et al.* 2014).

Sterk *et al.* (2013, henceforth SSH13) studied the relative importance of these three processes for different geostrophic wind regimes in an idealized situation. For high wind speeds ($U_g = 20\,\mathrm{m\,s^{-1}}$), turbulent mixing dominated over other process to control the SBL. With decreasing geostrophic wind, long-wave radiation divergence and especially surface coupling became relatively more important.

The first question we address here is how the relative significance of the processes holds for real cases, and we investigate similarities with the idealized case, with the focus on the more challenging low wind speed conditions. This is achieved using the SCM simulations with the set (d) forcings from Part 1 as a reference, and from there adjusting the intensity of the three processes.

Our second question concerns how these sensitivity runs compare with observations, and which processes may be responsible for a possible disagreement between the model output and observations. The process sensitivity is shown in so-called 'process diagrams', following SSH13 and Bosveld *et al.* (2014). Our third question is how do the process sensitivities compare for contrasting terrain types. For this we study whether possible variations in relative importance of the governing processes can be identified. In this way we aim to gain insight from this sensitivity analysis for possible future research fields.

The methodology of this analysis is described in section 3, after a short section on the model description in section 2. Section 4 discusses a model improvement concerning unphysical behaviour for specific humidity over snow. Results regarding the time series and vertical profiles are presented in section 5, while results regarding the process diagrams are presented in section 6. The discussion and conclusions follow in section 7.

2. Model description

The SCM used in our study is based on WRF version 3.2.1. A vertically stretched σ coordinate is used to determine the vertical levels, with the model top at a constant pressure level at an approximate height of 12 km. To minimize vertical resolution as a limiting factor, we apply 200 vertical levels, with the highest resolution close to the surface, and the first model level at about 0.55 m.

WRF offers many options for the parametrizations of the physical processes, which differ in their degree of complexity and computational efficiency. For the 3D and SCM runs, similar parametrizations were used as in the operational Antarctic Mesoscale Prediction System (NCAR UCAR, 2013; also Part 1). In the SCM simulations we switched off the micro-physics, since our focus is on clear skies and the observations during our study periods indicated mostly cloud-free conditions.

The turbulence physics within the model are represented with two possible schemes. Firstly the Mellor–Yamada–Janjic BL scheme (MYJ, Mellor and Yamada, 1982), which is a local, 1.5-order scheme that runs together with the Eta-similarity surface-layer scheme (Tastula and Vihma, 2011). This combination is considered appropriate for stable and slightly unstable flows (Hu *et al.*, 2010). Secondly we apply the YSU-BL scheme (Hong *et al.*, 2006; Hong, 2010), i.e. a first-order, non-local scheme, which runs together with the MM5-similarity surface-layer scheme (Skamarock *et al.*, 2008). The incorrect implementation of the stability function ϕ in WRF 3.2.1 was corrected in our study (S. Basu and W. Angevine, 2012; personal communications; SSH13; Hu *et al.*, 2013). Mixing is now reduced, which in some cases results in too stable SBLs (Sun and Barros, 2014; Kleczek *et al.*, 2014). Also the minimum friction velocity (u_*) that is artificially maintained by the model is lowered from 0.1 to $0.001\,\mathrm{m\,s^{-1}}$ for a more natural representation of atmospheric turbulence (Jiménez *et al.*, 2012).

We utilize the Noah land-surface model (LSM; Chen and Dudhia, 2001; Ek *et al.*, 2003), which uses four layers to represent the soil thermodynamics and takes soil, ice, and fractional snow cover effects into account, as well as surface emissivity properties (Skamarock *et al.*, 2008). The snow layer and the first soil layer are now both taken to be the top layer in Noah (Figure 2 in Part 1).

The atmospheric heating/cooling due to radiative flux divergence and the surface downward long-wave radiation is represented by the Rapid Radiative Transfer Model for GCMs (RRTMG). This scheme is a modification of the RRTM long-wave radiation scheme (Iacono *et al.*, 2008) and is a spectral-band scheme with 16 different bands.

3. Methodology

This section describes three parts of the methodology. The first part summarizes the general simulation setup for all SCM experiments (see also Part 1). The second part explains the strategy that was applied for the sensitivity analyses. The third part comments on the uncertainties in observations.

3.1. *General simulation set-up*

Part 1 reported on the different forcing methods for the SCM simulations. Set (d) forcings gave best results and is hence chosen as a reference here. The advection was determined from a WRF-3D simulation as the difference between the total tendency and the combined tendency by the physical processes.

The geostrophic wind speed U_g is assumed to be equal to the actual wind speed that was modelled with WRF-3D above a certain threshold height, since the actual wind speed is usually a good approximation of U_g poleward of the Tropics (Stull, 1988; Holton, 2004). This threshold height should be located sufficiently high above the BL and any low-level jet (LLJ) to avoid an unrealistically strong U_g which would falsely enhance inertial oscillations. For Cabauw this threshold height was 400 m, while for Sodankylä and Halley this was 300 m. Below the threshold height, U_g equals U_g at the threshold height.

In calm winds, the WRF model results are relatively sensitive to the snow-surface coupling (SSH13), which requires a thoughtful prescription of the surface characteristics. Hence, the snow depth is set equal to the observed snow depth. To improve on the surface characteristics, we adjusted the threshold snow depth, above which there is 100% snow cover for both WRF-3D and the WRF-SCM, such that the modelled albedo matches the observed albedo. As the SCM simulations are performed during night-time, it is not of interest to obtain a more realistic albedo, but the main goal is to improve on the snow surface characteristics.

3.2. *Sensitivity analysis strategy*

To quantify the sensitivity of the WRF-SCM to the parametrization of turbulent mixing, snow-surface coupling and long-wave radiation, we follow SSH13 (see below), but we extend this idealised study by comparing model results with observations. A similar sensitivity analysis was carried out by Bosveld *et al.* (2014) for the GABLS3 model intercomparison study.

In this real-world sensitivity analysis, we adjust the intensity of the three physical processes, and compare the results with the reference runs and observations. Apart from comparing representative thermodynamic profiles, we discuss so-called 'process diagrams' as introduced by Bosveld *et al.* (2014) and as applied in SSH13. A process diagram displays how the model state changes from the reference state to the state with perturbed process intensity. As such, two variables are plotted against each other, for which the variable is, in our case, either a time average over 9 h, or a change over 9 h. Hence the state of each simulation is represented by a single point in the process diagram. By drawing lines from the reference run to the simulations with adjusted process intensity, we can systematically compare the direction and length of the sensitivity lines for the three processes to learn more about their relative impacts.

The amount of turbulent mixing is adjusted by modifying the eddy diffusivities for momentum, heat, and moisture (K_m, K_h and K_q respectively) in the BL scheme by a constant (i.e. gain) factor. Simultaneously, the surface exchange coefficients (C_m, C_h and C_q respectively) in the surface-layer scheme are adjusted. Under low wind speed conditions, the model is more sensitive to adjusting both the turbulent mixing in the surface layer (SL) as well as within the BL scheme (SSH13) since the strongest temperature gradients are found within the SL. C_m is not directly determined within WRF so the friction velocity u_* was adjusted so that effectively C_m was altered in the same way as C_h and C_q. With the YSU scheme, u_* is also used to determine the eddy-diffusivity coefficients, for which we made a correction to avoid a double multiplication in the sensitivity study. Multiplication factors as in SSH13 have been used, being 0.25, 0.5, 2.0 and 4.0 as inspired by Cuxart *et al.* (2006), who showed that the maximum K_m and K_h vary roughly between 1 and 5 m^2 s^{-1} in a model intercomparison study. Hence, the selected uncertainty range captures the typical uncertainty in K. These runs are referred to as *mixing*.

The same multiplication factors are used for the snow thermal conductivity (λ_snow) (referred to as *coupling* runs). Observations indicate a large range of uncertainties in the snow/ice heat conductivity, which can vary in space (both horizontally and vertically) and time due to variations in snow/ice density and internal structure. Several λ_snow values have been reported, e.g. 0.078–0.574 for various snow densities (Sturm *et al.*, 2002), hourly values of 0.1–1.0 with average values of 0.4–0.5 for various sites (Huwald *et al.*, 2005), 0.02–0.3 for various sites (Gouttevin *et al.*, 2012) and 0.06–0.4 for various depths (Domine *et al.*, 2012). With the multiplication factors used in our modelling study, λ_snow varies from 0.032 to 0.51 for Cabauw and from 0.054 to 0.86 for Sodankylä and Halley (all W m^{-1} K^{-1}).

The amount of incoming long-wave radiation ($L\downarrow$) is adjusted by altering the initial q profile, since Zhang *et al.* (2001) and Svensson and Karlsson (2011) showed that $L\downarrow$ in very cold and dry clear-sky conditions is more sensitive to a small change in the q profile than a small change in the temperature profile. A smaller range of multiplication factors was used in this case, i.e. 0.5, 0.67, 1.5 and 2.0, because a larger perturbation could lead to unrealistic amounts of atmospheric q. We found that q varied from 0.79 to 11.3 g kg^{-1} for cloud-free conditions in winter (DJF) for measurements at De Bilt (Netherlands) for 1951–2014. With an initial $q = 1.6$ g kg^{-1} for the Cabauw case, we remain in the range of realistic q with these multiplication factors. Cloud-free DJF data for Sodankylä from December 2006 to December 2013 show a range of q from 0.08 to 4.66 g kg^{-1}. With an initial $q = 1.37$ g kg^{-1} this is also in the observed range after applying the multiplication factors. Studies at Halley indicated a range of monthly averages of 0.4–0.5 g kg^{-1} for the winter months (King and Anderson, 1999), and a median of about 0.34 g kg^{-1} for a 10-year winter climatology (2000–2009) (Nygård *et al.*, 2013). Since the initial q in our case (0.16 g kg^{-1}) is already below this range, decreasing q might be not as realistic, however we will include all permutations for completeness. The variation of initial $L\downarrow$ that we obtain by applying the permutation factors is 179–206 W m^{-2} for Cabauw (191 W m^{-2} for the reference case), 166–192 W m^{-2} for Sodankylä (reference = 178 W m^{-2}) and 124–144 W m^{-2} for Halley (reference = 134 W m^{-2}). Svensson and Karlsson (2011) found a comparable variation of > 20 W m^{-2} for $L\downarrow$ for clear-sky conditions in their study with nine global climate models during the Arctic winter (DJF). The simulations with adjusted q will be referred to as *q–radiation*.

We note that altering q affects not only $L\downarrow$, but may also affect the surface evaporation and thereby the surface energy balance and air temperature. Therefore, a change in model behaviour may not only be due to the $L\downarrow$ impact. $L\downarrow$ can alternatively be forced by adjusting the CO_2 gas concentration, as in McNider *et al.* (2012) and Bosveld *et al.* (2014). In these simulations we use 50 and 1500 ppmv instead of the reference 379 ppmv (as in Bosveld *et al.*, 2014). Although these concentrations are rather extreme, the simulations are meaningful to compare with *q-radiation* simulations. The ranges of realized $L\downarrow$ values are 183.0–197.4, 169.5–184.8 and 126.0–138.4 W m^{-2} for Cabauw, Sodankylä and Halley respectively. These runs will be referred to as CO_2-*radiation*.

3.3. *Observation uncertainties*

When comparing model simulations with observations, one needs to consider the reliability, the measurement uncertainty and the representativeness of the observations. Especially in cold and/or very stable conditions, measuring atmospheric variables may be challenging (e.g. Tjernström *et al.*, 2014). Equipment is more subject to failure, and turbulence is weak which hampers accurate flux measurements (Jacobs *et al.*, 2008; Lazzara *et al.*, 2012; Mikolajczyk *et al.*, 2012).

Therefore the measurement uncertainties will be shown in the process diagrams. Regarding the temperature observations, the uncertainty estimate amounts to ±0.2 °C for the 2 m temperature (T_{2m}), following Andreas *et al.* (2010) for the Surface Heat Budget of the Arctic Ocean (SHEBA) campaign. The measurement uncertainty of the T_{2m} difference in time is taken as twice the uncertainty in T_{2m} (±0.4 °C), as that is the maximum uncertainty that can occur. For the skin temperature (T_{skin}), Andreas *et al.* (2010) quantified an uncertainty of ±0.5 °C, while Langer *et al.* (2011) report an uncertainty of ±1 °C for the T_{skin} in a north Siberian winter, which will also be adopted here. The measurement uncertainty of the average difference between T_{2m} and T_{skin} is at most ±1.2 °C, taking into account uncertainties of both variables.

Uncertainties are also found in the flux observations. Westermann *et al.* (2009) found an uncertainty for the conductive heat flux (G) of ≈30% at Svalbard, which will be adopted here, while Town *et al.* (2008) found an uncertainty of ±2.6 to ±3.8 W m^{-2} for snow at the South Pole for a nine-year dataset. These uncertainties are within the 30% of the observed G from our study. Regarding $L\downarrow$, Marty *et al.* (2003) found an absolute uncertainty of ±2 W m^{-2} in Arctic winter, while Persson *et al.* (2002) and Vihma *et al.* (2009) report an uncertainty of ±4 W m^{-2} for the net long-wave radiation, which is used here. For the sensible heat flux (H) uncertainty, Vickers *et al.* (2010) found an absolute value of about 3–6 W m^{-2} for fluxes around 0 W m^{-2} for mature and young pine and maize. Though their surfaces excluded snow, we adopt the uncertainty of 6 W m^{-2}, as this might give a better indication of the flux uncertainty than using a relative uncertainty as e.g. in Andreas *et al.* (2010).

We did notice that the observed energy balance did not close, though we did not take into account the additional terms as in Heusinkveld *et al.* (2004). Though often the observed energy balance does not close when the turbulent fluxes are based on eddy-covariance measurements (Foken, 2008b; De Roode *et al.*, 2010; Steeneveld *et al.*, 2011) and the fluxes combined are not totally able to explain the available energy, uncertainties in the fluxes could be larger than the error bars in the presented process diagrams.

Besides the measurement uncertainties, the comparison of model results with observations is subject to 'representation errors' when observations are not representative of the model average grid cells. Tolk *et al.* (2008) state that representation errors in the SBL are relatively large due to unresolved topography with coarse model resolutions (for CO_2 in their case). We must keep in mind that observations can be strongly influenced by local processes, which are not captured by the model results representing grid averages. This could play a role in the WRF-3D simulations from which the advection was determined, despite their relatively high resolution of 4 × 4 km.

4. Air-snow moisture transport in YSU

We first address the problem of the unrealistic amount of humidity with the YSU BL scheme (solid line in Figure 1 for the Cabauw case) as was found in Part 1. Although a temperature inversion developed over time in the SBL, the specific humidity profile remained unaffected, which is inconsistent with the simulated negative latent heat flux (L_vE).

An investigation of the WRF code revealed that the moisture flux that is provided to the YSU-BL scheme is actually equal to 0 W m^{-2} when snow is present and L_vE calculated by the land-surface model directed towards the surface. This issue has been fixed in the WRF-SCM simulations here in Part 2. Appendix A gives more details on this technical issue.

Figure 1 shows the impact of this bug-fix on the YSU simulations for the Cabauw case. The humidity inversion is now able to develop more realistically. This also influences the

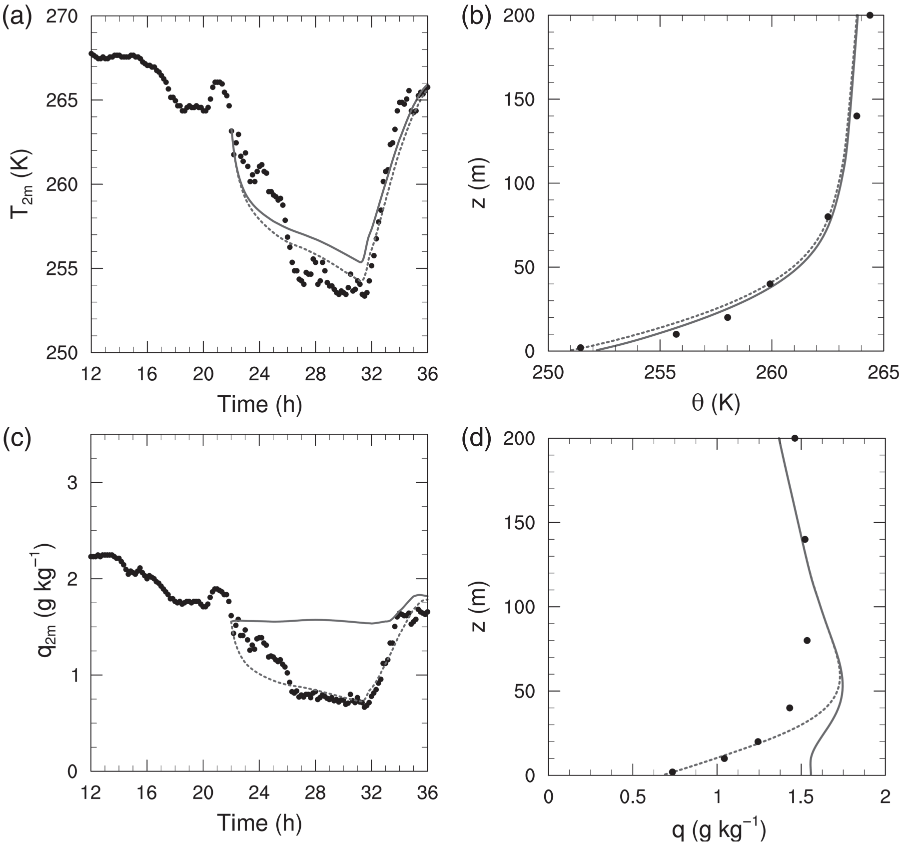

Figure 1. Time series of the WRF-SCM simulations with the YSU-BL scheme and observations for (a) the 2 m temperature (T_{2m}, K) and (c) the specific humidity (q_{2m}, g kg^{-1}) and the vertical structure after 9 h of the WRF-SCM simulation of (b) the potential temperature θ (K), and (d) the specific humidity q (g kg^{-1}) for Cabauw. The time in (a) and (c) is since 0000 UTC on 3 February 2012. The solid line gives the simulation with the erroneous moisture flux in YSU, and the dotted line gives the simulation with corrected moisture flux. The observations are represented by the black dots.

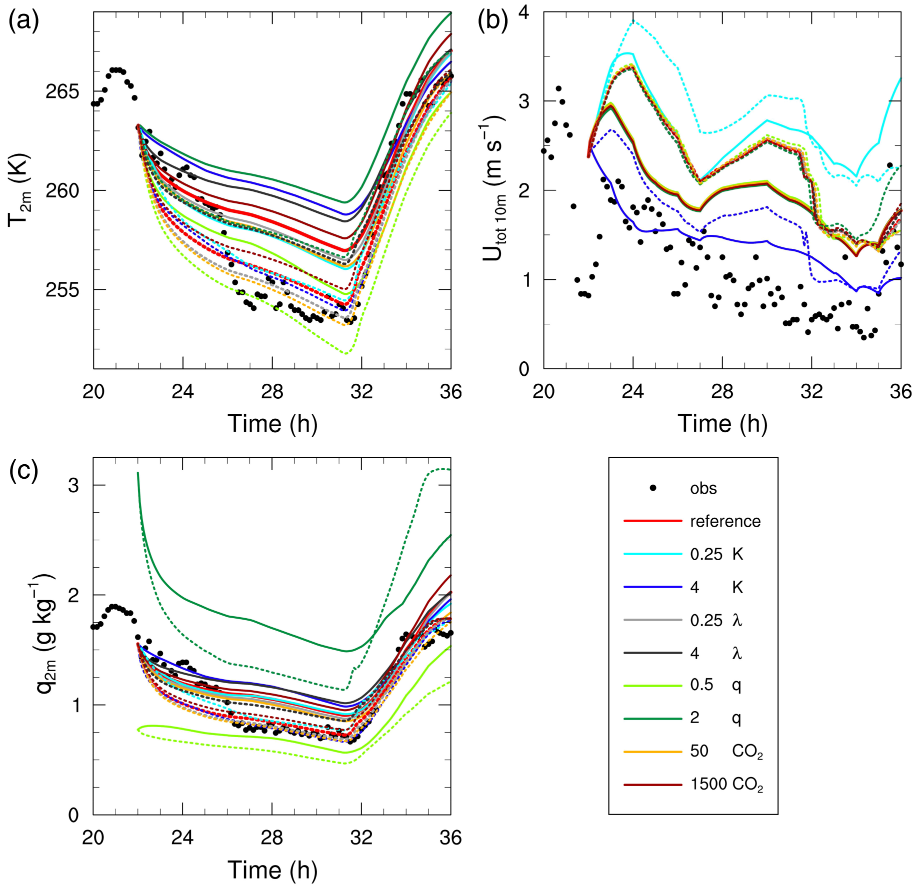

Figure 2. Time series of the WRF-SCM simulations and observations for (a) the 2 m temperature (T_{2m}, K) and (c) specific humidity (q_{2m}, g kg^{-1}), and (b) the total 10 m wind speed ($U_{tot\,10m}$, m s^{-1})) for Cabauw. Time is since 0000 UTC on 3 February 2012. Solid lines are for simulations with the MYJ-BL scheme, and dotted lines for simulations with the YSU scheme. K represents the change in mixing in both boundary and surface layer, λ represents the snow heat conductivity and thus the coupling, q represents the specific humidity profile and therefore the incoming long-wave radiation, and CO_2 represents the amount of CO_2 in ppmv and therefore also the incoming long-wave radiation. The observations are represented by the black dots.

near-surface temperature, with lower values, while the impact on the wind speed profile is minor (not shown).

Here in Part 2, we will use the simulations with the correct moisture flux from the atmosphere to the surface. Note that this adjustment did not influence the conclusions regarding how forcings should be described as discussed in Part 1. Hence we proceed with this set-up in combination with forcings following set (d) (varying Ug in time, and prescribing advection for temperature, humidity and momentum; see Part 1).

5. Time series and vertical profiles

In this section, we study the time series (Figure 2) of T_{2m}, the humidity at 2 m (q_{2m}) and the 10 m wind speed ($U_{tot\,10m}$) and the profiles after 9 h of simulation (Figure 3) of θ, wind speed U_{tot} and q. To limit the number of lines, only the findings with the maximum perturbations from the reference are shown (i.e. 0.25 and 4.0 for mixing and coupling, 0.5 and 2.0 for q-radiation, and the 50 and 1500 ppmv for CO_2-radiation). Note that the time series are only depicted for Cabauw, since in general analogous model behaviour was found for Sodankylä and Halley.

5.1. Temperature

Increasing the mixing intensity (dark blue lines in Figures 2 and 3) results in a more efficient exchange of warm and cold air, generating θ profiles with less curvature. With YSU (dotted dark blue) linear or concave-down profiles are simulated close to the surface. Decreased mixing (light blue lines) results in a stronger concave-up shaped θ profile.

We find that the near-surface air temperature increases with enhanced mixing and decreases with reduced mixing for MYJ (solid lines, respectively, approximately 1.9 K higher and 1.0 K lower than the reference at 2 m, 31 h, at Cabauw). A counter-intuitive behaviour was found with YSU where the 2 m temperature decreases with enhanced mixing and vice versa (∼0.4 K lower with enhanced mixing and 0.3 K higher with reduced mixing at 2 m, 31 h, Cabauw). Due to the low amount of mixing, the BL becomes very shallow. Then, taking the lowest mixing intensity simulation as a reference, extra mixing will result in relatively more upward mixed cold air, which is insufficiently compensated for by downward mixed warm air. This occurs with small eddy sizes and a stronger θ gradient close to the surface than higher up. As a result T_{2m} is higher for a lower amount of mixing. T_{skin} does decrease with reduced mixing for both MYJ and YSU as expected. This nonlinear behaviour regarding near-surface temperatures was also modelled by McNider *et al.* (2012) and SSH13 and found in observations (Acevedo and Fitzjarrald, 2003; Lüpkes *et al.*, 2008; Rinke *et al.*, 2012).

Enhanced coupling (dark grey lines), also results in a higher T_{2m} (∼1.5 and 2.2 K higher with MYJ and YSU, respectively, at 31 h, Cabauw), a higher θ and weaker concave-up shaped θ profiles. With increased (decreased) λ_{snow}, heat from the underlying medium is more (less) effectively brought towards the surface. This temperature signal is transferred to the atmosphere, leading to weaker (stronger) stratification. The impact of coupling is strongest at Halley, where the snow cover is 100% and a change in λ_{snow} is a maximum, while at Cabauw and Sodankylä the signal is smaller due to a smaller snow depth. Furthermore, the formulation that Noah LSM applies for sea-ice and ice shelves assumes λ for the underlying layers to be equal to λ_{snow}. A test with a λ equal to 2.2 W m^{-1}K^{-1} (ice heat conductivity as specified in Noah LSM) showed that the impact of the conductivity of the deeper layers was negligible.

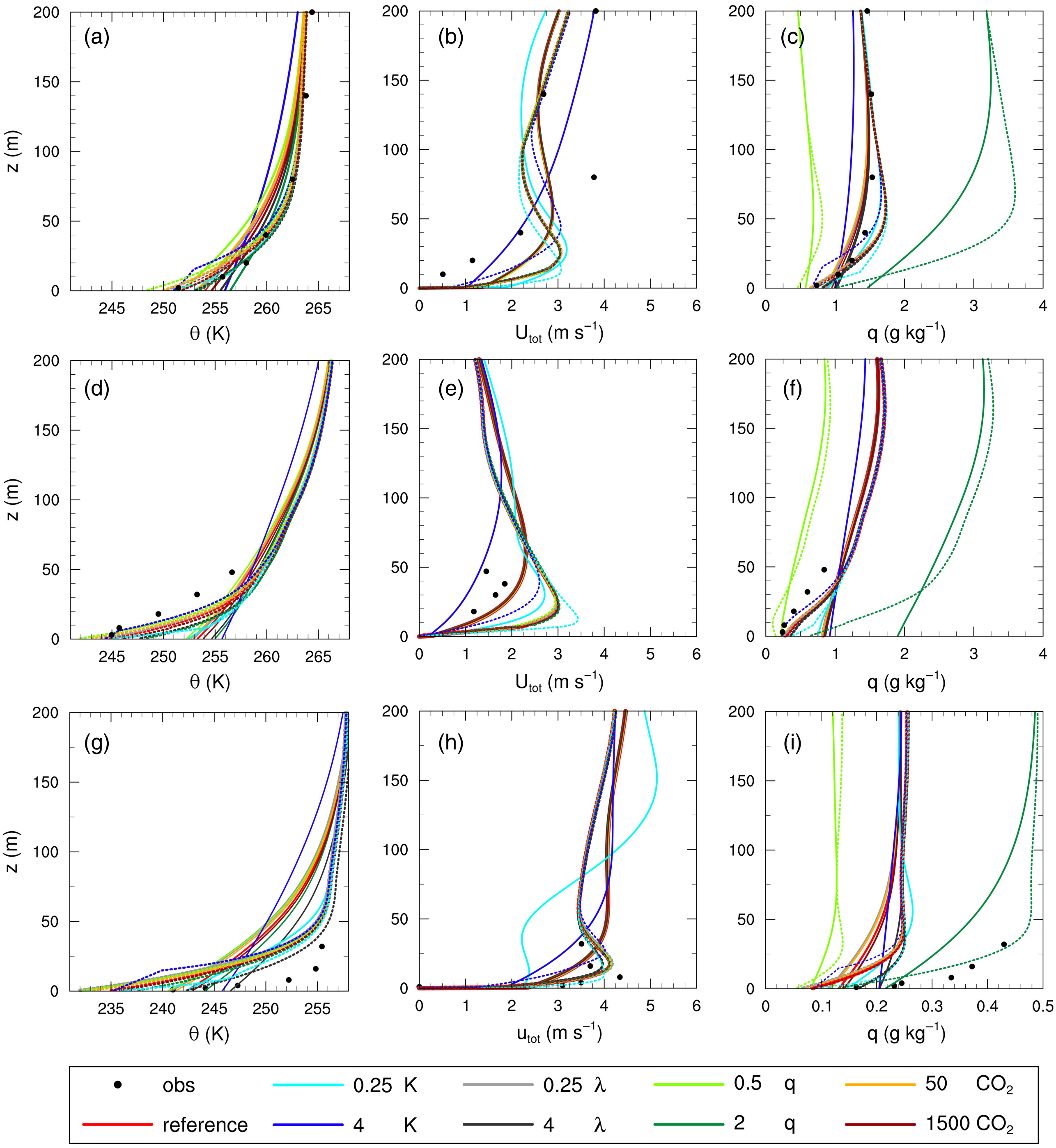

Figure 3. Vertical structure after 9 h of WRF-SCM simulation of the potential temperature θ (K), the total wind speed U_{tot} (m s^{-1}), and the specific humidity q (g kg^{-1}) for (a–c) Cabauw, (d–f) Sodankylä and (g–i) Halley. The axes range is kept similar for each variable for straightforward comparison, except for q at Halley since these values are considerably smaller than at the other sites. Solid lines are for simulations with the MYJ-BL scheme, dotted lines for simulations with YSU. Other details are as Figure 2.

Finally, an increase in $L\downarrow$ either by amplifying the initial q (dark green lines) or CO$_2$ (dark red lines) enhances T_{skin}, which is transported into the atmosphere, leading to higher temperatures and a weaker stratification. The opposite occurs when $L\downarrow$ is decreased.

Decreasing the process intensities provides θ profiles in closer agreement with Cabauw observations, as the near-surface inversion strength (e.g. up to 30 m) increases, though then with YSU the temperatures can become slightly too low. However, decreasing $L\downarrow$ is not a preferred solution since $L\downarrow$ was already underestimated (not shown). The YSU simulations perform best, and especially the 0.25 K run follows the observations accurately (Figure 3(a)), though they initially underestimate $T_{2\mathrm{m}}$ up to almost 2.9 K at 24 h (Figure 2(a)). For Sodankylä MYJ results improve with lowered process intensities. Near-surface temperatures are best forecast with YSU, although the overall inversion strength remains too strong (Figure 3(d)). Inversion strengths along the tower also improve for Halley with decreased process intensities, and the best θ shapes are again obtained with YSU, though the inflection point in the simulated θ profile is at a too high level (around 50 m, while in the observations this appears to be just below 20 m) and in general the θ values are too low (Figure 3(g)). For YSU the 0.25 K run predicts the θ better than the reference run, while an accurate forecast is also made when coupling is enhanced.

5.2. *Wind speed*

The model sensitivity on the simulated wind fields is most clear with an altered mixing process (Figures 2(b) and 3(b,e,h)). With enhanced mixing (dark blue lines), the LLJ disappears with MYJ (solid lines, also at other hours), while it is located at a higher altitude with YSU (dotted lines, also at other hours). At the 10 m level the strengthened mixing leads to lower wind speeds (up to $\sim 1\,\mathrm{m\,s^{-1}}$ lower for both BL schemes at Cabauw; Figure 2(b)). This improves the agreement with observations for Cabauw and Sodankylä, though at Halley $U_{\mathrm{tot\,8m}}$ is now underestimated by $\sim 1-2.4\,\mathrm{m\,s^{-1}}$. Reduced mixing (light blue lines) leads to higher $U_{\mathrm{tot\,10m}}$ than the reference case (up to 0.9 and $0.8\,\mathrm{m\,s^{-1}}$ higher with MYJ and YSU, respectively, at Cabauw). Similar results are found for Sodankylä and Halley, though at Halley wind speeds slightly lower than in the reference case are simulated at the end of the study period. The wind speed profiles indicate that the LLJ is now located at a lower altitude and is intensified at Cabauw and Sodankylä, whereas at Halley the LLJ is less elevated and intense (although more at an earlier stage). As diurnal effects at Halley are not strong at this time of year, the LLJ may be less intense.

The impact of reduced $L\downarrow$ (light green for q runs, orange for CO_2 runs) on wind speed is minimal. A slightly higher $U_{\mathrm{tot\,10m}}$ is found (Figure 2(b), less than $0.1\,\mathrm{m\,s^{-1}}$ for decreased q with YSU, smaller with CO_2 and for MYJ), which is explained by the slightly stronger stratification. Differences are clearer in q-radiation experiments than in CO_2-radiation experiments, due to a more strongly perturbed $L\downarrow$.

The effect of altered coupling on wind speed is also very small. As with the modified $L\downarrow$, increased (decreased) coupling results in decreased (increased) stratification and slightly more (less) exchange with the surface. At Halley this is seen in the weaker LLJ when applying YSU with increased coupling (Figure 3(h)).

Overall, the wind speed profiles and $U_{\mathrm{tot\,10m}}$ are most sensitive to the mixing intensity, since a change in K_m and C_m has a more direct impact on the wind profile.

While decreased mixing results in more accurate temperature simulations compared to observations, this produces a stronger overestimation of the 10 m wind speed forecast. Only with YSU at Halley does the modelled wind speed profile improve with the $0.25\,K$ run.

5.3. *Specific humidity*

The strongest response on q_{2m} (Figure 2(c)) and the q profiles (Figure 3(c,f,i)) is obtained by the q-radiation simulations (green lines), as a direct result of the modified initial q profile. Both an increase in $L\downarrow$ (via CO_2) and enhanced coupling lead to a slight q increase, by 0.05 and $0.12\,\mathrm{g\,kg^{-1}}$, respectively, at Cabauw. The higher air temperatures allow for more moisture than in the reference case, and dew formation is slightly smaller. Conversely, a q reduction is found for reduced CO_2-radiation and coupling (orange and light grey lines respectively).

Strengthened mixing with MYJ (solid dark blue lines) raises the near-surface q (with $0.14\,\mathrm{g\,kg^{-1}}$ at 2 m for Cabauw), with weakened q inversions. Enhanced mixing with YSU (dotted dark blue lines) again induces a counter-intuitive q_{2m} reduction. When mixing is enhanced at these low mixing intensities, more relatively dry air is mixed upwards than relatively moist air is mixed downwards. This is also related to the stronger concave-up shaped q profile with decreased mixing compared to enhanced mixing. This behaviour is similar to that of the near-surface temperature, as explained in section 5.1. Conversely, for decreased mixing with YSU we find an increased near-surface humidity coinciding with stronger humidity gradients. Interestingly, this nonlinear behaviour is now confirmed with MYJ for Cabauw and Halley.

When we compare the q simulations with observations, the YSU reference case with its relatively strong inversion (red dotted lines) captures the shape of the q inversion along the tower better than the MYJ reference for all sites (Figure 3(c,f,i)). Decreasing the mixing with MYJ (solid light blue lines) does improve the modelled profile shape, though at Cabauw and Sodankylä q is somewhat overestimated, while q remains underestimated at Halley (except at the surface). Decreasing mixing with YSU is also beneficial for Halley, but worsens results for Sodankylä and Cabauw. Decreasing CO_2-radiation and coupling also leads to stronger q inversions, when q decreases with the lower temperatures, but then for Cabauw skills at higher levels decrease with MYJ, while at Halley skills deteriorate for all levels by modelling a too low q. Decreasing q-radiation improves q at the surface for Sodankylä, but then the profile shape again is wrongly forecast. Increasing q-radiation improves the q profile at Halley; both the profile shape and values at higher levels are better simulated (Figure 3(i)).

6. Process diagrams

This section discusses the process diagrams as described in section 3.2, which show selected variables for coupling, radiation and mixing. Each will be studied separately in the following subsections.

The process diagrams in Figures 4–6 show a sensitivity analysis for two reference runs, MYJ in green and YSU in red, from which lines are drawn indicating the altered intensities for the three processes (solid lines for MYJ, dotted lines for YSU).

6.1. *Snow-surface coupling*

First we focus on the snow-surface coupling in Figure 4. Here the amount of cooling at 2 m during the 9 h simulation is presented versus the average G to examine the time-integrated interaction between the surface and the atmosphere. The general positioning of the observations in the process diagrams for Cabauw and Sodankylä indicates that a stronger cooling coincides with a stronger conductive heat flux due to a larger temperature gradient through the snow layer. At Halley some heating at the 2 m level occurs by heat advection (Part 1), while the snow heat flux remains negative.

Overall, we find that the process of $L\downarrow$ follows the trend of decreased G with decreased cooling in time for all locations, e.g. with increased $L\downarrow$, T_{skin} increases leading to a smaller temperature gradient and hence smaller G. A similar behaviour is seen with adjusted mixing with MYJ. Then, with increased mixing, more warm air from higher levels is brought towards the surface and cold air is brought upwards, so that the temperature gradient decreases and G becomes smaller. The direction of the coupling lines are perpendicular to these by mixing and radiation. When λ_{snow} is increased, G increases, though at the same time more heat from the underlying medium is transported to the surface leading to less cooling in time wich counteracts the effect on G due to the stronger λ_{snow}.

Note that the general orientation of the process sensitivity lines, apart from the mixing orientation with YSU (next subsection), is similar to that found with the Regional Atmospheric Climate Model (RACMO) SCM in Bosveld *et al.* (2014) for the Cabauw site but without snow and with higher wind speeds. The relative contributions differ, but this makes sense since different multiplication factors have been applied, while additionally the conductivity of the soil was also adjusted in Bosveld *et al.* (2014), which is not done in our study. The general orientation is also comparable to the idealized case-study in SSH13, which reassures us that their findings for an idealized case are also applicable for real cases.

6.1.1. *MYJ versus YSU*

We find some differences between the two sensitivity analysis sets from the default MYJ (solid lines) and YSU (dotted lines) simulations. The overall picture for coupling and radiation is similar, but differs for mixing. In the YSU runs, the mixing orientation is perpendicular to the MYJ mixing orientation, as was found by McNider *et al.* (2012) and SSH13. In these studies, decreased mixing resulted in less cooling at the 2 m level and

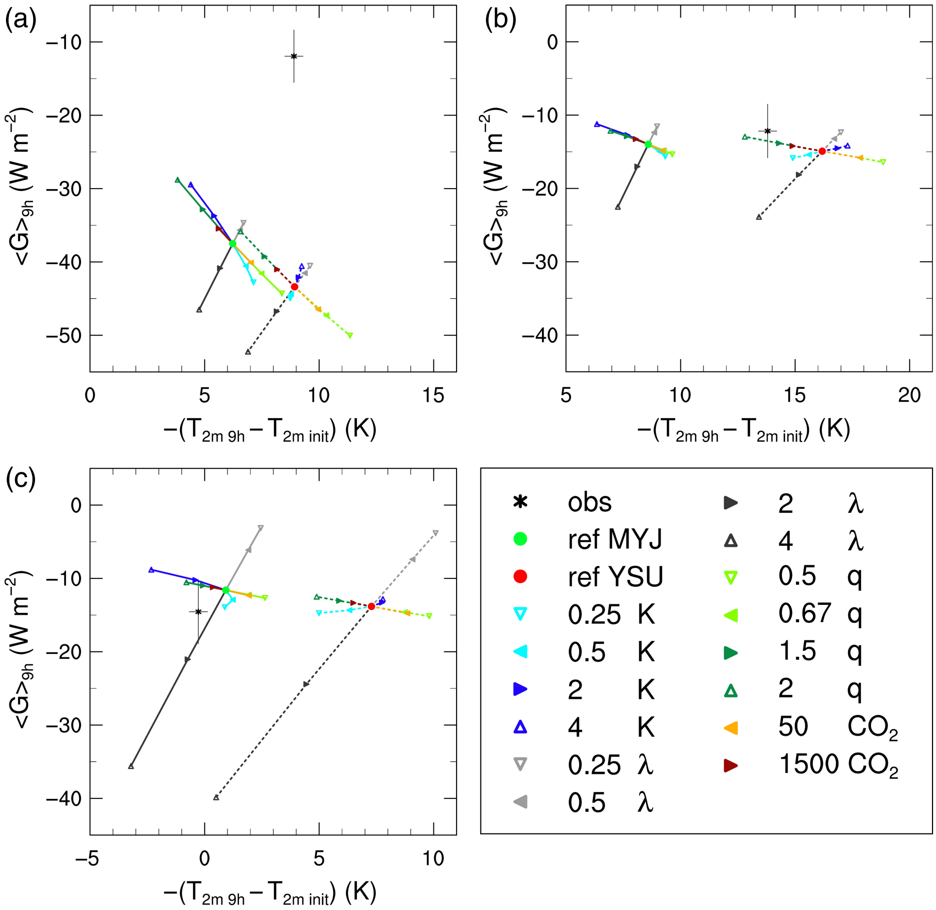

Figure 4. Cooling of the 2 m temperature ($-(T_{2\mathrm{m}\,9\mathrm{h}} - T_{2\mathrm{m}\,\mathrm{init}})$, K) over 9 h versus the soil heat flux ($< G >_{9\mathrm{h}}$, W m^{-2}) averaged over 9 h for (a) Cabauw, (b) Sodankylä and (c) Halley. ref MYJ is the reference for the simulations with the MYJ-BL scheme (solid lines) and ref YSU is the reference for the simulations with the YSU-BL scheme (dashed lines). The asterisk with error bars represents the observation with its measurement uncertainties in the error bar. Other details are as Figure 2.

vice versa (section 5.1). We refer to this mixing behaviour as 'nonlinear' as both an increase and decrease in $T_{2\mathrm{m}}$ can be found for a similar direction of mixing adjustment. Interestingly, this nonlinear behaviour is well captured with the YSU-BL scheme but not as clearly with MYJ. With MYJ, $T_{2\mathrm{m}}$ did increase slightly at the very end of the study period at Halley when wind speeds also drop strongly, so that for the $T_{2\mathrm{m}}$ difference over 9 h this nonlinearity is clear. This is no longer visible for the average $T_{2\mathrm{m}}$ over the entire period (Figure 5). This nonlinear behaviour mostly occurred with light winds and low mixing (McNider *et al.*, 2012; SSH13). YSU produces a stronger stratified BL with smaller eddy diffusivity than MYJ (Figure 3), hence showing the nonlinear behaviour more clearly. Evidently, the artificial minimum background diffusivity in MYJ is responsible for this phenomenon, as its reduction reveals this nonlinearity, and results in eddy diffusivities comparable to those obtained with YSU (not shown). Since observations support the existence of this nonlinearity, it is promising that it can be reproduced in both model schemes.

In addition, YSU appears to be more sensitive to radiation variations than MYJ (green and brown/orange lines), as indicated by the longer process lines, especially for Sodankylä and Halley (Figure 4). Though $L\downarrow$ is similar in MYJ and YSU, the impact of a change in $L\downarrow$ is larger when T_{skin} is lower, as is the case with YSU compared to MYJ.

Also, YSU appears to be more sensitive to variations in coupling than MYJ. At Halley T_{skin} is already about 4 K lower with the reference YSU than with the reference MYJ run, and therefore a change in λ_{snow} has a stronger influence on T_{skin} due to the larger temperature gradient through the top snow layer. For Cabauw and Sodankylä the differences in coupling-line length are smaller, due to the patchy snow cover and, in the case of Cabauw, smaller snow depth. Furthermore, the coupling lines of YSU have a smaller slope: e.g. a larger change in cooling for a fixed change in G, such that the coupling impact seems to be larger here.

6.1.2. *Site intercomparison*

The general direction of the process orientation for the three sites is comparable, but the strength of the sensitivity varies between the sites. Firstly, for the mixing and radiation processes, the change in G per change of cooling is a lot more profound for Cabauw than for the other sites, i.e. the lines are steeper. This could be related to the method of determining G in the WRF model:

$$G = -\lambda \frac{\Delta T}{\Delta z_{\mathrm{tot}}}, \tag{1}$$

where ΔT is the temperature difference across the total depth of the top layer (Δz_{tot}), being the sum of the snow cover (Δz_{snow}) and the top soil layer (Δz_{soil}), and λ is the conductivity of the top layer (Appendix B).

All parameters in Eq. (1) vary for the three locations, since Δz_{tot} amounts to 8.5, 67 and 43.75 cm for Cabauw, Sodankylä and Halley, respectively (Figure 2 in Part 1). As a consequence, the effective resolution in the underlying medium varies between sites, hampering a straightforward comparison. Savijärvi (2013) has shown that the near-surface temperatures are sensitive to the resolution in the snow pack, since coarser resolution leads to higher T_{skin} and $T_{2\mathrm{m}}$.

Furthermore, λ differs between the sites due to the different snow cover and vegetation fractions. For Cabauw with 83% snow cover and 85% vegetation, a λ of 0.27 W m^{-1}K^{-1} is simulated. For Sodankylä with 55% snow cover and 49% vegetation, this is 0.42 W m^{-1}K^{-1}. For Halley with snow over sea-ice, WRF sets the

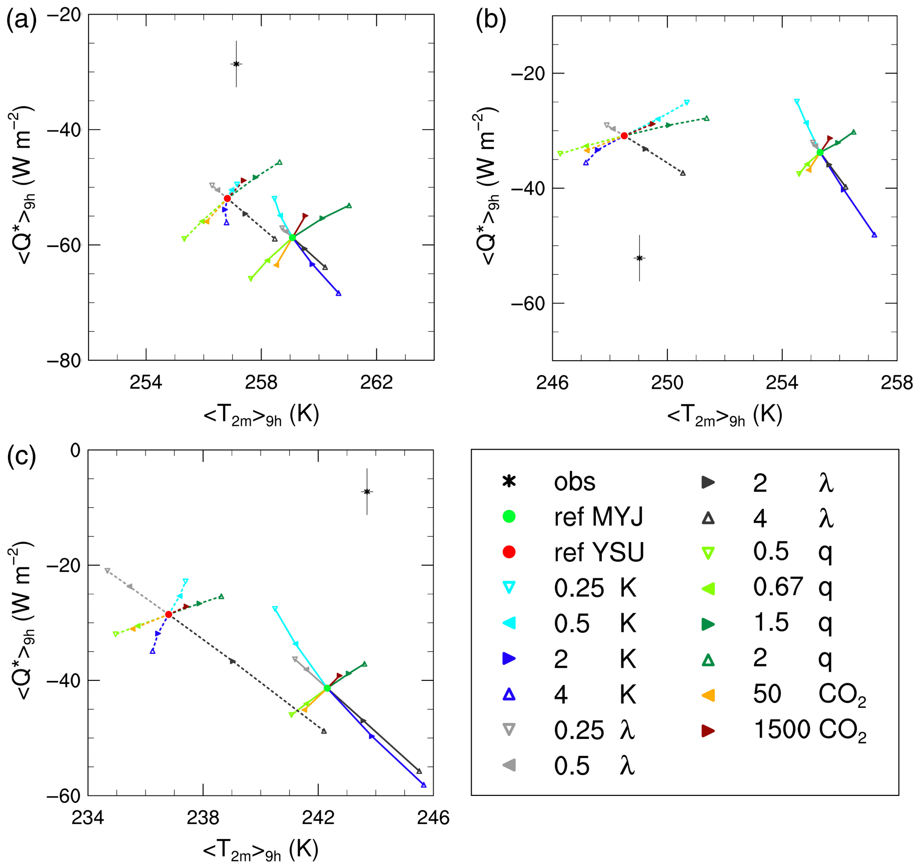

Figure 5. The 2 m temperature ($< T_{2m} >_{9h}$, K) versus the net radiation ($< Q^{*} >_{9h}$, W m^{-2}), both averaged over 9 h for (a) Cabauw, (b) Sodankylä and (c) Halley. Other details are as Figure 4.

snow cover to 100% while additionally the conductivity of the underlying layers is set to the snow conductivity, such that λ is 0.21 W m^{-1}K^{-1}. Therefore, the relative impact of altering λ_{snow} on the total λ is most relevant for Halley, since for Cabauw and Sodankylä the relative impact of the underlying and unchanged $\lambda_{\text{soil+veg}}$ is larger due to the smaller snow-cover and the relatively large λ_{soil} (also Appendix B). This stronger coupling impact for Halley compared to the other sites is also clearly visible with the longer coupling lines in Figure 4. Though actually ΔT throughout the first soil layer and λ are smaller for Cabauw than for Sodankylä, this is divided by a smaller Δz, so that the impact of a change in ΔT on G is expected to be largest for Cabauw.

In addition, the length of the radiation lines differs between sites: they are largest for Cabauw and smallest for Halley. This is explained by the higher q at Cabauw and hence larger $L\downarrow$ changes (section 3.2), when equal multiplication factors are applied for the three sites. The effect of mixing is slightly larger for Halley than for Sodankylä, but this could be related to the somewhat stronger wind speeds present in this particular Halley case.

6.1.3. *Comparison with observations*

At Cabauw G is greatly overestimated, which is partly explained by the fact that WRF applies an equation for λ_{snow} which gives higher values for a certain snow density compared to what we used to estimate the observed values, e.g. for fresh snow with a density of 100 kg m^{-3}, a λ_{snow} of 0.128 W m^{-1}K^{-1} is utilized (where we used 0.021 W m^{-1}K^{-1} for Cabauw observations), while for snow with density 200 kg m^{-3}, a λ_{snow} of 0.215 W m^{-1}K^{-1} is modelled (we used 0.084 W m^{-1}K^{-1} for Sodankylä observations). Savijärvi (2013) also reported on the strong impact of the selected density and conductivity on the (near-)surface temperatures, especially in stable conditions. Figure 4 confirms that reducing λ_{snow} brings the model results closer to the observations for Cabauw and Sodankylä, though for the latter G is only slightly overestimated. On the other hand, it must be noted that the Sodankylä measurement site is more heterogeneous than the other two sites. G is determined through the top 2 cm of the snow layer, which implies that G is determined for a full snow cover, although there are also trees present, so that G representative for the entire site could be larger. The same holds for Cabauw, where some grass may still stick through the snow cover. For Halley the simulated λ_{snow} equals λ_{snow} used for observations, but now G is slightly underestimated, so apparently $\Delta T/\Delta z$ is too small in the model.

Furthermore, the model formulation for G is not identical to the way that the observed G was determined, which can cause some differences between observed and modelled G. We expect the differences to be smaller when the relative contribution of the snow depth is larger.

Regarding the cooling in time, we see that for Cabauw and Sodankylä better results are found with YSU. Also for Halley, more cooling is found with YSU, but now the temperature is strongly underestimated. This is also seen in the profiles in Figure 3.

6.2. *Long-wave radiation*

The process diagrams in Figure 5 represent the process of radiation where the net radiation ($Q*$) versus T_{2m} is depicted, both averaged over 9 h. $Q*$ is defined as $L\downarrow$ minus $L\uparrow$ at the surface. Therefore, with higher surface temperatures, $L\uparrow$ will be larger, and with higher air temperatures and/or specific humidity, $L\downarrow$ will be larger.

In general, with enhanced coupling, T_{skin} increases which also leads to higher atmospheric temperatures. Hence both $L\uparrow$ and $L\downarrow$ increase. However, the enhanced $L\uparrow$ dominates over the enhanced $L\downarrow$, which thus results in a more negative $Q*$. The opposite is found for reduced coupling. The MYJ mixing process follows the same orientation as the altered coupling process, while for YSU the nonlinear behaviour is seen in T_{2m}, as described in the previous sections. With decreased YSU mixing, $L\downarrow$ increases due to higher atmospheric temperatures, while $L\uparrow$ decreases with lower T_{skin}, resulting in a less negative $Q*$. Considering the perturbation of radiation when $L\downarrow$ is reduced, less energy reaches the surface leading to lower $T_{2\mathrm{m}}$. This also results in less $L\uparrow$, however since $Q*$ becomes more negative, the decreased $L\downarrow$ dominates over the decreased $L\uparrow$. With enhanced radiation, the opposite is found.

6.2.1. *MYJ versus YSU*

Next, we discuss the sensitivity to radiation perturbation for the two BL schemes. The difference between the mixing orientations was already explained. Moreover, the radiation lines are 'flatter' with YSU than with MYJ. Considering that the differences in $L\downarrow$ between MYJ and YSU are not that large, this means that $L\uparrow$ plays a relatively more important role in the YSU runs than in the MYJ runs. The stronger changes in $L\uparrow$ also follow from the stronger changes in $T_{2\mathrm{m}}$ and T_{skin} (not shown).

As with the coupling process diagrams (Figure 4), the YSU runs are also more sensitive to coupling than MYJ, which is seen from the longer lines. The large temperature gradient through the top layer induces a profound impact of an altered λ_{snow} on the surface temperature. Also (most clear for Sodankylä and Halley), the coupling line is more 'flat' with YSU than with MYJ, since again $L\downarrow$ is comparable, but with lower temperatures the impact on $L\uparrow$ is smaller for a similar change in T_{skin}.

6.2.2. *Site intercomparison*

The impact of mixing with MYJ is larger for Sodankylä than for Cabauw, and even larger for Halley, since the orientation is similar but the lines are longer. This is related to the stronger θ stratification at Halley (Figure 3). Subsequently, when mixing is modified, the temperature change is greater than cases with weaker stratification. Furthermore, the near-surface wind speed is highest for Halley (winds may more easily accelerate with the low roughness length over the smooth snow cover), which can also partly explain the more efficient mixing. This cannot explain the difference in mixing efficiency between Cabauw and Sodankylä, since wind speeds at Sodankylä are a bit lower than at Cabauw. Then differences in mixing sensitivity are most likely due to the stronger temperature stratification at Sodankylä. With YSU, the differences in the relative importance of mixing between the three sites are not so clear due to the changing orientation in YSU mixing. Again we see for Halley a stronger impact of the coupling process as found before.

6.2.3. *Comparison with observations*

Comparing the model results with the observations reveals that for Cabauw and Halley $|Q*|$ is substantially overestimated. Temperatures close to the surface are overestimated for Cabauw with MYJ but are of the right order with YSU, though for Halley these temperatures are mostly underestimated. Reducing $T_{2\mathrm{m}}$ with less coupling and less MYJ mixing brings the modelled $Q*$ closer to the observed value, but then temperatures are too low (especially for Halley). Lowering $T_{2\mathrm{m}}$ by reducing $L\downarrow$ is not advised, because $L\downarrow$ is already strongly underestimated for Cabauw and Halley (up to about 30 W m^{-2} for both cases). Note that at Cabauw, when θ is predicted nicely and q is somewhat overestimated with the 0.25 K YSU simulation (Figure 3(a)–(c)), light blue dotted lines), $L\downarrow$ is still underestimated, which indicates an incorrectness in the radiation schemes (Wild *et al.*, 2001; Niemelä *et al.*, 2001; and section 7). $L\downarrow$ is overestimated by up to 8 W m^{-2} for the Sodankylä reference case with MYJ but less with YSU. Though the $T_{2\mathrm{m}}$ and $L\downarrow$ for YSU are simulated almost correctly for Sodankylä, still $|Q*|$ is underestimated. With a too strong stratification with YSU, T_{skin} becomes too low (especially at the start of the simulation), leading to an underestimated $L\uparrow$ on average.

For Cabauw and Sodankylä, a closer agreement with observed $T_{2\mathrm{m}}$ and $Q*$ is obtained with YSU than with MYJ. Due to the weaker connection with the surface with YSU (smaller H and a lower eddy diffusivity in the BL), a stronger stratification is found explaining the better performance for $T_{2\mathrm{m}}$ and $Q*$.

Regarding the relative contribution of the processes, it appears that, for this set of variables, mixing is relatively important for the sites with stronger temperature stratification. Again, coupling seems to be relatively important for Halley, while radiation plays a prominent role for Cabauw.

6.3. *Turbulent mixing*

Atmospheric mixing is presented in the last process diagrams, where H versus the temperature difference between 2 m and the surface are displayed, both averaged over 9 h of simulation (Figure 6). Overall, when coupling and radiation strengthen, more energy is available at the surface, resulting in a smaller temperature difference, causing H to decline, and vice versa. Modified mixing produces a line perpendicular to this orientation, due to that H is directly affected by the altered eddy diffusivities and exchange coefficients. So when mixing increases, a larger H is found and vice versa. More mixing enhances the surface heat exchange, resulting in a smaller temperature difference close to the surface (which somewhat counteracts the increase in H) and vice versa.

6.3.1. *MYJ versus YSU*

Comparing the mixing lines of MYJ and YSU (blue solid and dotted lines, respectively), the change in H is smaller for a similar temperature difference with YSU. Apparently the counteracting process of reduced temperature gradient with enhanced mixing is relatively stronger with YSU than with MYJ, whilst eddy diffusivities are larger with MYJ than YSU, which reflects directly in H when multiplying K.

As with the mixing process, the lines of radiation and coupling are also flatter with YSU than with MYJ for Cabauw and Halley, but vice versa for Sodankylä. However, also the relative orientation of the line through the origin and the reference point is different: for Cabauw and Halley the reference YSU is more flat, while for Sodankylä the MYJ reference is more flat. The coupling and radiation processes more or less follow this reference orientation (for YSU this deviates more than for MYJ).

Of note is that the atmospheric θ stratification seems smaller with MYJ than with YSU for all sites (Figure 3). However, the process diagrams indicate a larger difference between $T_{2\mathrm{m}}$ and T_{skin} for MYJ for all locations. This is explained by the relatively larger eddy diffusivities K with MYJ than with YSU, combined with relatively small exchange coefficients C, i.e. the ratio K/C is larger with MYJ than with YSU. Then the BL is able to mix, e.g. heat more efficiently in the BL with the larger K yielding relatively higher temperatures in the BL, but the surface layer cannot keep up with this efficient mixing with the smaller C, and thus the temperature difference between the surface and the first model level becomes rather large. Thus it seems that YSU has a more consistent transition from the surface-layer exchange coefficients to BL eddy diffusivities than MYJ. As mentioned by Svensson and Holtslag (2009), one should be careful in matching the surface layer and BL parametrizations. This deficiency in MYJ may be enhanced by the imposed background diffusivity in the BL which may not match with the lower limit on the exchange coefficients in the surface layer.

6.3.2. *Site intercomparison*

It appears that the strength of the model sensitivity differs for the three sites. Regarding the mixing lines, for both BL schemes these are steepest for Cabauw (i.e. strongest change in H per dT), and flattest for Sodankylä (weakest change in H per dT). The other process sensitivities are not as straightforward: with

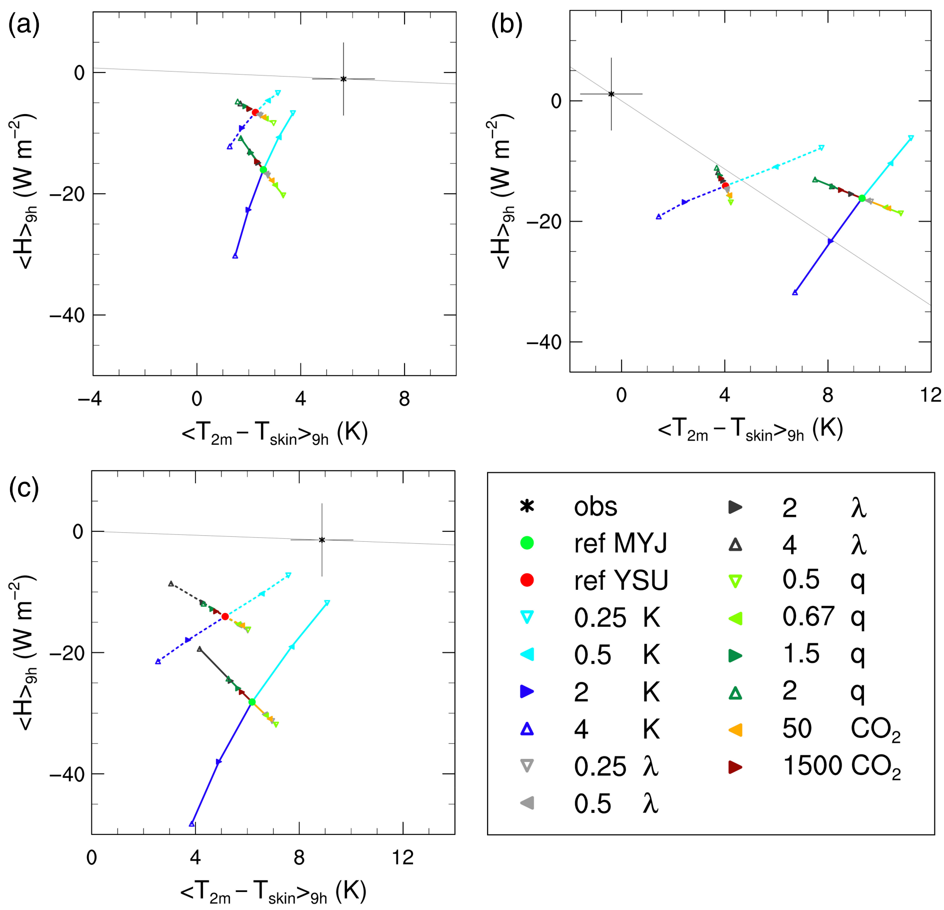

Figure 6. The temperature difference between the 2 m level and the surface ($< T_{2m} - T_{skin} >_{9h}$, K) versus the sensible heat flux ($< H >_{9h}$, W m^{-2}), both averaged over 9 h for (a) Cabauw (where the observed H is averaged over only the first 4h due to an incomplete dataset), (b) Sodankylä and (c) Halley. The lines through the observational points and the origin connect all points with a similar mixing as observed. Other details are as Figure 4.

YSU radiation and coupling are flattest for Cabauw and steepest for Sodankylä, while with MYJ this is opposite. Also the relative position of the reference points compared to the origin differs. E.g., the reference point compared to the origin is already flatter with YSU for Cabauw and Halley, and flatter with MYJ for Sodankylä, so that when radiation and coupling lines follow more or less the same mixing strength as the reference run, this results in flatter lines as well.

Again, the impact of radiation is larger for Cabauw and Sodankylä than for Halley, while for Halley the impact of coupling is strongest. Mixing seems also somewhat more important for this set of variables for Sodankylä and Halley, possibly due to the stronger stratifications found here and hence the stronger impact on temperatures close to the surface when the mixing intensity is modified.

6.3.3. Comparison with observations

In these stable conditions, the magnitude of H is small. For Cabauw, the dataset of H was incomplete for the duration of the night and is therefore averaged over only the first 4 h (black asterisk). The model simulations overestimate H, though the temperature gradient remains underestimated. Decreased mixing brings the model simulations closer in agreement with the measured H, and also improves the temperature gradient.

The observed H at Sodankylä is slightly positive with a positive temperature gradient between the surface and 2 m. Though the lowest two model levels in the θ profile indicate a stable stratification, the gradient is a bit smaller than for the higher tower levels, since the lower part of the tower is surrounded by trees. Moreover, the Sodankylä site is rather heterogeneous. Measurements of T_{2m} and the radiation components and hence T_{skin} are from a more open site than H measured along the tower between trees. The WRF-SCM simulations overestimate the magnitude of H and dT. With YSU a slightly smaller H magnitude is forecast, combined with a smaller temperature gradient, than with MYJ. For both BL schemes, decreasing the mixing does give a smaller H, though this overestimates the temperature gradients even more.

For Halley, the observed H has small magnitudes, which are overestimated by the model together with an underestimated ΔT. YSU yields a closer agreement with the observed H, while MYJ yields a closer agreement with the observed ΔT. Reducing mixing brings the simulations closer to observations.

Finally, the eddy-covariance measurements are located at 3 m at Cabauw, 8 m at Sodankylä and 4 m at Halley, i.e. not *a priori* in the constant flux layer (Foken, 2008a), or the lower 10% of the BL. The observed LLJ at Halley is at around 8 m (Figure 3(h)), which suggests the BL height to be at around the same height. For Sodankylä the LLJ is somewhat higher, but clearly below 80 m. Thus the measured H could be underestimating H closer to the surface.

7. Discussion and conclusions

This study presents the relative importance of snow-surface coupling, downward long-wave radiation, and turbulent mixing on the development of the stable boundary layer (SBL) over snow, using the WRF single-column model. The focus is on clear-sky conditions with low wind speeds. Three different snow cases over grass (Cabauw, The Netherlands), forest (Sodankylä, Finland) and an ice shelf (Halley, Antarctica, modelled as sea ice in WRF) are presented. Part 1 of the overall study covered an evaluation of the SCM simulations for varying forcings. The sensitivity analysis presented here is performed by varying the intensity of the three processes, for the simulation with optimized forcings taken from Part 1.

The sensitivity analysis was performed for both MYJ and YSU BL schemes. With increased mixing, the magnitude of the sensible heat flux (H) increased, and potential temperature (θ) and q inversions weakened. The LLJ was less developed and at a higher altitude. The resulting smaller surface cooling lead to smaller conductive snow-heat fluxes (G), larger outgoing long-wave radiation ($L\uparrow$), and a more negative net radiation ($Q*$). With increased snow conductivity, we found less cooling in time at the 2 m level and a more negative $Q*$. The impact of coupling on the q profile was very small (except for Halley), while the impact was negligible for wind speed. With increased $L\downarrow$, θ and q inversions also weakened, resulting in smaller G and H. The wind profiles were not very sensitive to the altered $L\downarrow$. Opposite results were found with reduced process intensities.

Concerning differences between the MYJ and YSU BL schemes, we found:

- Stronger atmospheric θ stratifications with YSU than with MYJ, while stratifications over the surface layer were strongest for MYJ. This followed from a larger eddy-diffusivity/exchange-coefficient ratio in MYJ.
- H changed more profoundly in MYJ than in YSU for a given $T_{2\mathrm{m}} - T_{\mathrm{skin}}$. This implies that the eddy diffusivity is more efficient in MYJ, and that (e.g.) with enhanced mixing, a stronger counteracting behaviour of reduced temperature gradient is seen in YSU.
- With YSU, a counter-intuitive behaviour of temperature for very low mixing intensities: $T_{2\mathrm{m}}$ decreased for increased mixing and vice versa. With very light turbulence, cold air was not mixed upward sufficiently. Therefore, $T_{2\mathrm{m}}$ remained higher than when mixing was increased. MYJ captured this behaviour only weakly for Halley. Reducing the background diffusivity did show the nonlinearity with MYJ. Additionally, both schemes showed a similar nonlinear behaviour for near-surface q.

Regarding the relative importance of the processes for the various sites, we conclude that:

- The radiation impact was relatively large for Cabauw and Sodankylä, most obviously so when q was adjusted.
- Coupling was relatively more important for Halley. In the sea-ice code in WRF, the entire underlying medium is set to the snow heat conductivity; this causes a higher impact if this variable is changed. Furthermore, the snow cover was 100% at Halley, about 83% at Cabauw and 55% at Sodankylä. Therefore the influence of the unchanged underlying medium was larger for the last two sites, reducing the impact of the modified snow heat conductivity.

Note that some differences between the sites could also occur, because the atmospheric conditions were not equal during the three case-studies. Furthermore, the depth of the top layer differs for the three sites, because it is a composite of the snow depth and the first soil layer in the WRF model. For the comparison between the three locations, a similar resolution would be desirable. However, in this study we aimed to compare the WRF model behaviour as it is, without making too many modifications to the code.

Besides studying the process sensitivities, we aimed to quantify whether altered process intensities improved the model results compared to observations. We found that:

- G was greatly overestimated for Cabauw due to the model's higher snow heat conductivity. Also, G was calculated on the basis of temperature observations assuming full snow cover (which was not true for Cabauw and Sodankylä), while WRF determines G from the snow layer and half of the top soil layer. We recommend a revised snow heat conductivity formulation in the WRF model, to circumvent the too high conductivities.
- $Q*$ was strongly underestimated for Cabauw and Halley even for runs which gave realistic θ- and q profiles, hinting at a deficiency in the long-wave radiation scheme. This underestimation was also found with numerical weather prediction models by Niemelä *et al.* (2001) for clear-sky winter conditions in Sodankylä, especially for strong inversions, as well as by Wild *et al.* (2001) for general circulation models. The latter attribute this to a problem in the simulation of the thermal emission from cold, dry and cloud-free atmospheres. Barton *et al.* (2014) also suspect other reasons than the modelled temperature and humidity for the bias, since several models forced with the same profiles of temperature and humidity still show a large spread in clear-sky downward long-wave radiation.
- The magnitude of H was overestimated by the WRF-SCM. However, the measured $|H|$ might have been underestimated as the instrument might have been located above the very shallow surface layer.
- The θ stratification at the surface was underestimated for Cabauw and Halley. At Sodankylä the θ stratification between the surface and the 2 m level was overestimated using data from the automatic weather station in open land. The Sodankylä tower in a forested area indicated that the stratification was underestimated with MYJ and overestimated with YSU.

Overall, we conclude that for most variables the WRF-SCM skill improves when mixing was decreased, mostly so for the YSU-BL scheme due to the stronger θ and q inversion along the towers (though temperatures were still strongly underestimated at Halley). Unfortunately, the wind speed skill mostly deteriorated with decreased mixing. This indicates that SBL simulations may be improved by adjusting the eddy diffusivities and exchange coefficients independently for momentum and scalars. Under very stable conditions, the Prandtl number (K_m/K_h) may diverge from unity, to account for momentum transport due to pressure fluctuations (Kim and Mahrt, 1992). For a MYJ and a quasi-normal scale elimination (QNSE) BL scheme intercomparison, Tastula *et al.* (2015) found a high sensitivity of the model results to the choice of the turbulent Prandtl number for neutral stratification. They noticed that in the Monin–Obukhov similarity function for heat, the choice of this Prandtl number can be more important than the functional form of the similarity function itself, though the relative importance of the latter does increase with increasing near-surface stability.

Decreasing the coupling also improved the temperature and moisture gradients without strongly affecting the wind field, though the impact was less strong than reducing mixing. Decreasing $L\downarrow$ also yielded stronger gradients, but this is not recommended due to the already underestimated $L\downarrow$. Considering the reservations about the observations in cold conditions, as mentioned in section 3.3, it is difficult to make firm conclusions about the model results compared with observations from these particular cases. However, obviously not only the different schemes but also the process intensities heavily influence the performance of the WRF-SCM. Some analyses of the time-averaging dependency for the process diagrams are given in Appendix C.

Finally we notice that we prescribed advection for temperature, humidity and momentum as obtained from Part 1. Here in Part 2, the same advection was prescribed for the simulations with modified process strengths, although the advection was estimated from WRF-3D runs without any adjusted process intensity. We recommend an analogous study in a 3D model, when the advection would adjust itself accordingly.

Acknowledgements

We thank Dr Reinder Ronda (Wageningen University) for his valuable discussions regarding WRF-related issues. Furthermore, we would like to thank the Royal Netherlands Meteorological

Institute, the Finnish Meteorological Institute and the British Antarctic Survey for the observational data used in this study. We thank the ECMWF for the boundary conditions that were used in the WRF-3D simulations. We acknowledge the support from NWO with grant 829.09.005 and 863.10.010 and the Academy of Finland (grants 263918 and 283101).

Appendix A

Erroneous moisture flux in YSU

A peculiar behaviour of humidity was found in the simulations with the YSU-BL scheme. The sensible and latent heat fluxes were directed downwards, and while a temperature inversion would develop, this was not the case for the humidity. Studying the WRF code revealed a problem in the definition of the moisture flux when snow is present and the potential evaporation (E_p) is negative (towards the surface). While a latent heat flux is calculated by the Noah land-surface model, the flux signalled to YSU remains 0 W m^{-2}, so that no atmospheric humidity is actually transported to the surface. This explains why the surface-based humidity inversion does not develop. The slight changes in humidity in time that were seen in the profiles and time series were caused by the prescribed advection.

The technical problem is explained as follows. The moisture flux that is provided to YSU (*qfx* in the code) equals the latent heat flux in kg m^{-2}s^{-1} calculated in the Noah LSM (*ETA_KINEMATIC* in the code, here E_{kin}). When snow is present, E_{kin} is defined as:

$$E_{\text{kin}} = E_{\text{snow}}\sigma_{\text{snow}} + (E_{\text{dir}} + E_{\text{c}} + E_{\text{tt}})\,(1 - \sigma_{\text{snow}})\,, \tag{A1}$$

where E_{snow} represents the sublimation from the snow pack, σ_{snow} equals the snow fraction, and E_{dir}, E_{c}, and E_{tt} represent the direct soil evaporation, the canopy water evaporation and the total plant transpiration respectively. However, all these terms are only calculated when E_p is larger than 0, so for an upward moisture flux. Indeed the Noah LSM calculates the latent heat flux in the form of dew-fall (or frost-fall) when $E_p \leq 0$ (*DEW* in the code; $DEW = -E_p \cdot 0.001$ with E_p also in kg m^{-2}s^{-1}), but not the actual terms necessary in Eq. (A1), and thus E_{kin} remains 0 W m^{-2}.

This problem was reported to the WRF helpdesk, and is fixed in module_sf_noahlsm.F from version 3.7 onwards (J. Dudhia, 2015; personal communication) by including the *DEW* term in Eq. (A1), such that:

$$\begin{aligned} E_{\text{kin}} =& E_{\text{snow}}\sigma_{\text{snow}} + (E_{\text{dir}} + E_{\text{c}} + E_{\text{tt}})\,(1 - \sigma_{\text{snow}}) \\ &- 1000.0\,DEW, \end{aligned} \tag{A2}$$

and will be checked upon for the glacier and sea-ice noah-modules for the next WRF release (likely version 3.8, J. Dudhia, 2015; personal communication). In this way, the moisture flux that is signalled from the Noah LSM to the YSU-BL scheme is equal to E_p, and moisture is truly transported from the atmosphere to the surface.

Appendix B

Noah LSM top layer conductivity

The heat conductivity of the top layer, λ, as in Eq. (1) is composed as follows in the Noah land surface model used in WRF (Ek *et al.*, 2003):

$$\begin{aligned} \lambda = & \sigma_{\text{snow}}\lambda_{\text{snow+soil+veg}} \\ & + (1 - \sigma_{\text{snow}})\lambda_{\text{soil+veg}}, \end{aligned} \tag{B1}$$

$$\lambda_{\text{snow+soil+veg}} = \frac{\Delta z_{\text{snow}}}{\Delta z_{\text{tot}}}\lambda_{\text{snow}} + \frac{\Delta z_{\text{soil}}}{\Delta z_{\text{tot}}}\lambda_{\text{soil+veg}}, \tag{B2}$$

$$\lambda_{\text{soil+veg}} = \lambda_{\text{soil}} exp(-\beta_{\text{veg}}\sigma_{\text{veg}}), \tag{B3}$$

where σ_{snow} is the snow cover fraction. $\lambda_{\text{snow+soil+veg}}$ is the conductivity of the soil with vegetation and snow cover and determined as in Eq. (B2). λ_{snow} depends on the snow density which also changes over time. $\lambda_{\text{soil+veg}}$ is the conductivity of the soil with vegetation without snow cover, which is determined with the bare soil conductivity λ_{soil} in combination with an empirical coefficient β_{veg} and the vegetation fraction σ_{veg} in Eq. (B3).

Appendix C

Process diagrams: temporal evolution

In this article we have discussed the process diagrams which are obtained after 9 h of simulation. However, sometimes a variable changes very rapidly over time at the start of the simulation, which is now averaged out over the 9 h. Hence, it is also interesting to see the development of the process diagrams over time, which is done in this Appendix. The process diagrams throughout the first hour, first 5 h and first 9 h are given in Figures S1–S3. These correspond to the time averages taken over the first hour, first 5 h, and first 9 h, respectively, where the latter is equal to the process diagrams in Figures 4–6.

First we discuss the snow-surface coupling process diagrams (average G versus $T_{2\text{m}}$ cooling in time (Figure S1). In general for Cabauw and Sodankylä, we see more cooling over time, combined with a stronger snow heat flux due to a larger temperature gradient in the soil. This is not as straightforward for Halley, where advection plays a more important role.

Regarding the sensitivity lines, we find most clearly for the first few hours for Cabauw and Sodankylä that the change in G per change in cooling becomes smaller with time, i.e. the slope of the lines decreases. This holds both for observations and sensitivity analysis lines, where the latter is also seen for Halley. Just after the start of the simulation, a stronger drop in T_{skin} is found, which causes a stronger $\Delta T/\Delta z$ in the soil, while it takes a bit more time to transfer this signal to the 2 m level. Therefore initially the change in G is larger with a similar cooling at 2 m, resulting in steeper lines in the top figures in Figure S1.

The process diagrams for the long-wave radiation process over time ($Q*$ versus $T_{2\text{m}}$, both averaged over time) are shown in Figure S2. The general trend in time is that $T_{2\text{m}}$ decreases, and $Q*$ becomes less negative, as we would expect. For Halley this is not the case for the observations. Here, the position of the observation remains the same, due to the strong advection in combination with the already present polar night (see also Part 1, $T_{2\text{m}}$ stayed around 244 K). For MYJ at Halley, $T_{2\text{m}}$ and $Q*$ also stay rather similar. For YSU there was indeed a stronger decrease in $T_{2\text{m}}$, as was also seen in Part 1 with the reference case, combined with a less negative $Q*$ due to a smaller $L\uparrow$.

The change in $Q*$ becomes smaller over time with a similar variation in $T_{2\text{m}}$, so a ‘flattening’ of the lines is seen for all sites and each process. This is because at the start of the simulation the strongest impact is at the surface to which $L\uparrow$ is directly linked, while it takes some time before this signal is transferred to the 2 m level.

Finally the process diagrams through time for the turbulent mixing process (H versus the temperature difference between 2 m and the surface, both averaged in time) are shown in Figure S3. For Cabauw, the orientation of the observed lines stays similar over time, though the temperature gradient and the H magnitude do decrease with time. For Sodankylä the observations turn around the origin, thus changing the orientation. Since both variables are very close to 0, the observations are very sensitive to measurement uncertainties regarding the sign. For Halley, the orientation changes slightly with an increase in altered H per dT (i.e. the line steepens).

Concerning the orientation of the radiation and coupling process with YSU over time, we find the same orientation for Cabauw, a larger change in H per dT (steeper line) for Sodankylä, and a smaller change per dT (flatter line) for Halley. The YSU mixing line becomes more flat with time for all sites (smaller change in H per dT, most clear for Sodankylä and Halley). On the other hand, the MYJ mixing line shows a steepening of the line. The MYJ radiation and coupling orientations stay roughly constant with time for all locations. Furthermore, for all sites the impact of radiation with MYJ and YSU decreases with time (line length decreases). This also holds for the mixing process with YSU for Cabauw and Sodankylä. It could be that the relative impact of the processes decreases with time, because the strongest changes in e.g. T_{skin} are found in the beginning of the runs. Therefore, the impact averages out after more hours, when changes in time are not as strong.

Supporting information

The following supporting information is available as part of the online article:

Figure S1. Process diagrams in time over x hours. Cooling of the 2 m temperature ($-(T_{2\mathrm{m}\,x\mathrm{h}} - T_{2\mathrm{m\,init}})$, K) over x h versus the soil heat flux ($< G >_{x\mathrm{h}}$, W m^{-2})) averaged over x h for (a,d,g) Cabauw, (b,e,h) Sodankylä and (c,f,i) Halley. K represents the change in mixing in both boundary and surface layer, λ represents the snow heat conductivity and thus the coupling, q represents the specific humidity profile and therefore the incoming long-wave radiation, and CO_2 represents the amount of CO_2 in ppmv and therefore also the incoming long-wave radiation. ref MYJ is the reference for the simulations with the MYJ-BL scheme (solid lines) and ref YSU is the reference for the simulations with the YSU-BL scheme (dashed lines). The asterisk with error bars represents the observation with its measurement uncertainties in the error bar.

Figure S2. Process diagrams in time over x hours. The 2 m temperature ($< T_{2\mathrm{m}} >_{x\mathrm{h}}$, K) versus the net radiation ($< Q^* >_{x\mathrm{h}}$, W m^{-2}), both averaged over x h for (a,d,g) Cabauw, (b,e,h) Sodankylä and (c,f,i) Halley. Other details are as Figure S1.

Figure S3. Process diagrams in time over x hours. The temperature difference between the 2 m level and the surface ($< T_{2\mathrm{m}} - T_{\mathrm{skin}} >_{x\mathrm{h}}$, K) versus the sensible heat flux ($< H >_{x\mathrm{h}}$, W m^{-2}), both averaged over x h for Cabauw (a,d,g for x=5 and x=9h, the observed H is only averaged over the first 4h due to missing data), Sodankylä (b,e,h) and Halley (c,f,i). The lines through the observational points and the origin connect all points with a similar mixing as observed. Other details are as Figure S1.

References

Acevedo OC, Fitzjarrald DR. 2003. In the core of the night –effects of intermittent mixing on a horizontally heterogeneous surface. *Boundary-Layer Meteorol.* **106**: 1–33, doi: 10.1023/A:1020824109575.

André JC, Mahrt L. 1982. The nocturnal surface inversion and influence of clear-air radiative cooling. *J. Atmos. Sci.* **39**: 864–878, doi: 10.1175/1520-0469(1982)039<0864:TNSIAI>2.0.CO;2.

Andreas EL, Persson POG, Jordan RE, Horst TW, Guest PS, Grachev AA, Fairall CW. 2010. Parameterizing turbulent exchange over sea ice in winter. *J. Hydrometeorol.* **11**: 87–104, doi: 10.1175/2009JHM1102.1.

Atlaskin E, Vihma T. 2012. Evaluation of NWP results for wintertime nocturnal boundary-layer temperatures over Europe and Finland. *Q. J. R. Meteorol. Soc.* **138**: 1440–1451, doi: 10.1002/qj.1885.

Baas P, Bosveld FC, Lenderink G, Van Meijgaard E, Holtslag AAM. 2010. How to design single-column model experiments for comparison with observed nocturnal low-level jets. *Q. J. R. Meteorol. Soc.* **136**: 671–684, doi: 10.1002/qj.592.

Barton NP, Klein SA, Boyle JS. 2014. On the contribution of long-wave radiation to global climate model biases in Arctic lower-tropospheric stability. *J. Clim.* **27**: 7250–7269, doi: 10.1175/JCLI-D-14-00126.1.

Beljaars ACM, Holtslag AAM. 1991. Flux parameterization over land surfaces for atmospheric models. *J. Appl. Meteorol.* **30**: 327–341, doi: 10.1175/1520-0450(1991)030<0327:FPOLSF>2.0.CO;2.

Bosveld FC, Baas P, Steeneveld GJ, Holtslag AAM, Angevine WM, Bazile E, de Bruijn EIF, Deacu D, Edwards JM, Ek M, Larson VE, Plein JE, Raschendorfer M, Svensson G. 2014. The third GABLS intercomparison case for evaluation studies of boundary-layer models. Part B: Results and process understanding. *Boundary-Layer Meteorol.* **152**: 157–187, doi: 10.1007/s10546-014-9919-1.

Chen F, Dudhia J. 2001. Coupling an advanced land surface-hydrology model with the Penn State-NCAR MM5 modelling system. Part I: Model implementation and sensitivity. *Mon. Weather Rev.* **129**: 569–585, doi: 10.1175/1520-0493(2001)129<0569:CAALSH>2.0.CO;2.

Cuxart J, Holtslag AAM, Beare RJ, Bazile E, Beljaars A, Cheng A, Conangla L, Ek M, Freedman F, Hamdi R, Kerstein A, Kitagawa H, Lenderink G, Lewellen D, Mailhot J, Mauritsen T, Perov V, Schayes G, Steeneveld GJ, Svensson G, Taylor P, Weng W, Wunsch S, Xu KM. 2006. Single-column model intercomparison for a stably stratified atmospheric boundary layer. *Boundary-Layer Meteorol.* **118**: 273–303, doi: 10.1007/s10546-005-3780-1.

Delage Y. 1997. Parameterising sub-grid scale vertical transport in atmospheric models under statically stable conditions. *Boundary-Layer Meteorol.* **82**: 23–48, doi: 10.1023/A:1000132524077.

De Roode SR, Bosveld FC, Kroon PS. 2010. Dew formation, eddy-correlation latent heat fluxes, and the surface energy imbalance at Cabauw during stable conditions. *Boundary-Layer Meteorol.* **135**: 369–383, doi: 10.1007/s10546-010-9476-1.

Domine F, Gallet JC, Bock J, Morin S. 2012. Structure, specific surface area and thermal conductivity of the snowpack around Barrow, Alaska. *J. Geophys. Res.* **117**: D00R14, doi: 10.1029/2011JD016647.

Edwards JM, McGregor JR, Bush MR, Bornemann FJ. 2011. Assessment of numerical weather forecasts against observations from Cardington: Seasonal diurnal cycles of screen-level and surface temperatures and surface fluxes. *Q. J. R. Meteorol. Soc.* **137**: 656–672, doi: 10.1002/qj.742.

Ek MB, Mitchell KE, Lin Y, Rogers E, Grunmann P, Koren V, Gayno G, Tarpley JD. 2003. Implementation of Noah land surface model advances in the National Centers for Environmental Prediction operational mesoscale Eta model. *J. Geophys. Res.* **108**: 8851, doi: 10.1029/2002JD003296.

Foken T. 2008a. *Micrometeorology*. Springer-Verlag: Berlin and Heidelberg, Germany.

Foken T. 2008b. The energy balance closure problem: An overview. *Ecol. Appl.* **18**: 1351–1367, doi: 10.1890/06-0922.1.

Gouttevin I, Menegoz M, Domin F, Krinner G, Koven C, Ciais P, Tarnocai C, Boike J. 2012. How the insulating properties of snow affect soil carbon distribution in the continental pan-Arctic area. *J. Geophys. Res.* **117**: G02020, doi: 10.1029/2011JG001916.

Heusinkveld BG, Jacobs AFG, Holtslag AAM, Berkowicz SM. 2004. Surface energy balance closure in an arid region: Role of soil heat flux. *Agr. Forest Meteorol.* **122**: 21–37, doi: 10.1016/j.agrformet.2003.09.005.

Holton JR. 2004. *An Introduction to Dynamic Meteorology*. Elsevier Academic Press: Amsterdam, Netherlands.

Holtslag AAM. 2006. GEWEX atmospheric boundary-layer study (GABLS) on stable boundary layers. *Boundary-Layer Meteorol.* **118**: 243–246, doi: 10.1007/s10546-005-9008-6.

Holtslag AAM, Svensson G, Baas P, Basu S, Beare B, Beljaars ACM, Bosveld FC, Cuxart J, Lindvall J, Steeneveld GJ, Tjernström M, Van De Wiel BJH. 2013. Stable atmospheric boundary layers and diurnal cycles –challenges for weather and climate models. *Bull. Am. Meteorol. Soc.* **94**: 1691–1706, doi: 10.1175/BAMS-D-11-00187.1.

Hong SY. 2010. A new stable boundary-layer mixing scheme and its impact on the simulated East Asian summer monsoon. *Q. J. R. Meteorol. Soc.* **136**: 1481–1496, doi: 10.1002/qj.665.

Hong SY, Noh Y, Dudhia J. 2006. A new vertical diffusion package with an explicit treatment of entrainment processes. *Mon. Weather Rev.* **134**: 2318–2341, doi: 10.1175/MWR3199.1.

Hu X-M, Klein PM, Xue M. 2013. Evaluation of the updated YSU planetary boundary layer scheme within WRF for wind resource and air quality assessments. *J. Geophys. Res. Atmos.* **118**: 10490–10505, doi: 10.1002/jgrd.50823.

Hu X-M, Nielsen-Gammon JW, Zhang F. 2010. Evaluation of three planetary boundary layer schemes in the WRF model. *J. Appl. Meteorol. Climatol.* **49**: 1831–1844.

Huwald H, Tremblay LB, Blatter H. 2005. Reconciling different observational data sets from Surface Heat Budget of the Arctic Ocean (SHEBA) for model validation purposes. *J. Geophys. Res.* **110**: C05009, doi: 10.1029/2003JC002221.

Iacono MJ, Delamere JS, Mlawer EJ, Shephard MW, Clough SA, Collins WD. 2008. Radiative forcing by long-lived greenhouse gases: Calculations with the AER radiative transfer models. *J. Geophys. Res.* **113**: D13103, doi: 10.1029/2008JD009944.

Jacobs AFG, Heusinkveld BG, Holtslag AAM. 2008. Towards closing the surface energy budget of a mid-latitude grassland. *Boundary-Layer Meteorol.* **126**: 125–136, doi: 10.1007/s10546-007-9209-2.

Jiménez PA, Dudhia J, Fidel Gonzlez-Rouco J, Navarro J, Montvez JP, Garca-Bustamante E. 2012. A revised scheme for the WRF surface layer formulation. *Mon. Weather Rev.* **140**: 898–918, doi: 10.1175/MWR-D-11-00056.1.

Kim J, Mahrt L. 1992. Simple formulation of turbulent mixing in the stable free atmosphere and nocturnal boundary layer. *Tellus* **44A**: 381–394, doi: 10.1034/j.1600-0870.1992.t01-4-00003.x.

King JC, Anderson PS. 1999. A humidity climatology for Halley, Antarctica, based on frost-point hygrometer measurements. *Antarct. Sci.* **11**: 100–104, doi: 10.1017/S0954102099000139.

Kleczek MA, Steeneveld GJ, Holtslag AAM. 2014. Evaluation of the weather research and forecasting mesoscale model for GABLS3: Impact of boundary-layer schemes, boundary conditions and spin-up. *Boundary-Layer Meteorol.* **152**: 213–243, doi: 10.1007/s10546-014-9925-3.

Langer M, Westermann S, Muster S, Piel K, Boike J. 2011. The surface energy balance of a polygonal tundra site in northern Siberia. Part 2: Winter. *Cryosphere* **5**: 509–524, doi: 10.5194/tc-5-509-2011.

Lazzara MA, Weidner GA, Keller LM, Thom JE, Cassano JJ. 2012. Antarctic automatic weather station program; 30 years of polar observations. *Bull. Am. Meteorol. Soc.* **93**: 1519–1537, doi: 10.1175/BAMS-D-11-00015.1.

Lüpkes C, Vihma T, Birnbaum G, Wacker U. 2008. Influence of leads in sea ice on the temperature of the atmospheric boundary layer during polar night. *Geophys. Res. Lett.* **35**: L03805, doi: 10.1029/2007GL032461.

Mahrt L. 1999. Stratified atmospheric boundary layers. *Boundary-Layer Meteorol.* **90**: 375–396, doi: 10.1023/A:1001765727956.

Mahrt L. 2014. Stably stratified atmospheric boundary layers. *Annu. Rev. Fluid Mech.* **46**: 23–45, doi: 10.1146/annurev-fluid-010313-141354.

Mahrt L, Sun J, Blumen W, Delany T, Oncley S. 1998. Nocturnal boundary-layer regimes. *Boundary-Layer Meteorol.* **88**: 255–278, doi: 10.1023/A:1001171313493.

Marty C, Philipona R, Delamere J, Dutton EG, Michalsky J, Stamnes K, Storvold R, Stoffel T, Clough SA, Mlawer EJ. 2003. Downward longwave irradiance uncertainty under arctic atmospheres: Measurements and modeling. *J. Geophys. Res.* **108**: 4358, doi: 10.1029/2002JD002937.

McNider RT, Steeneveld GJ, Holtslag AAM, Pielke RA Sr., Mackaro S, Pour-Biazar A, Walters J, Nair U, Christy J. 2012. Response and sensitivity of the nocturnal boundary layer over land to added longwave radiative forcing. *J. Geophys. Res.* **117**: D14106, doi: 10.1029/2012JD017578.

Mellor GL, Yamada T. 1982. Development of a turbulence closure model for geophysical fluid problems. *Rev. Geophys. Space Phys.* **20**: 851–875, doi: 10.1029/RG020i004p00851.

Mikolajczyk DE, Lazzara MA, Welhouse LJ, Keller LM, Thom JE, Tsukernik M, Cassano JJ. 2012. 'The Antarctic automatic weather station network: The challenges and rewards of making polar observations'. In *12th Conference on Polar Meteorology and Oceanography*, Seattle, WA. American Meteorological Society: Boston, MA. https://ams.confex.com/ams/12POLAR/webprogram/Paper225450.html (accessed 13 October 2015).

NCAR UCAR. 2013. 'Current AMPS configuration'. http://www2.mmm.ucar.edu/rt/amps/information/configuration/configuration.html (accessed 13 October 2015).

Niemelä S, Räisänen P, Savijärvi H. 2001. Comparison of surface radiative flux parameterizations. Part I: Longwave radiation. *Atmos. Res.* **58**: 1–18, doi: 10.1016/S0169-8095(01)00084-9.

Nygård T, Valkonen T. 2013. Antarctic low-tropospheric humidity inversions: 10-year climatology. *J. Clim.* **26**: 5205–5219, doi: 10.1175/JCLI-D-12-00446.1.

Persson POG, Fairall CW, Andreas EL, Guest PS, Perovich DK. 2002. Measurements near the Atmospheric Surface Flux Group tower at SHEBA: Near-surface conditions and surface energy budget. *J. Geophys. Res.* **107**: 8045, doi: 10.1029/2000JC000705.

Rinke A, Ma Y, Bian L, Xin Y, Dethloff K, Persson POG, Lüpkes C, Xiao C. 2012. Evaluation of atmospheric boundary-layer surface process relationships in a regional climate model along an East Antarctic traverse. *J. Geophys. Res.* **117**: D09121, doi: 10.1029/2011JD016441.

Savijärvi H. 2013. High-resolution simulations of the night-time stable boundary layer over snow. *Q. J. R. Meteorol. Soc.* **140**: 1121–1128.

Skamarock WC, Klemp JB, Dudhia J, Gill DO, Barker DM, Duda MG, Huang XY, Wang W, Powers JG. 2008. *A Description of the Advanced Research WRF Version 3*. Technical Note TN 475+STR. NCAR: Boulder, CO. http://www.mmm.ucar.edu/wrf/users/docs/arw_v3.pdf (accessed 13 October 2015).

Steeneveld GJ, Van de Wiel BJH, Holtslag AAM. 2006. Modeling the evolution of the atmospheric boundary layer coupled to the land surface for three contrasting nights in CASES-99. *J. Atmos. Sci.* **63**: 920–935, doi: 10.1175/JAS3654.1.

Steeneveld GJ, Tolk LF, Moene AF, Hartogensis OK, Peters W, Holtslag AAM. 2011. Confronting the WRF and RAMS mesoscale models with innovative observations in the Netherlands: Evaluating the boundary-layer heat budget. *J. Geophys. Res.* **116**: D23114, doi: 10.1029/2011JD016303.

Sterk HAM, Steeneveld GJ, Holtslag AAM. 2013. The role of snow-surface coupling, radiation, and turbulent mixing in modeling a stable boundary layer over Arctic sea ice. *J. Geophys. Res. Atmos.* **118**: 1199–1217, doi: 10.1002/jgrd.50158.

Sterk HAM, Steeneveld GJ, Vihma T, Anderson PS, Bosveld FC, Holtslag AAM. 2015. Clear-sky stable boundary layers with low winds over snow-covered surfaces. Part 1: WRF model evaluation. *Q. J. R. Meteorol. Soc.* **141**: 2165–2184, doi: 10.1002/qj.2513.

Stull RB. 1988. *An Introduction to Boundary-Layer Meteorology*. Kluwer Academic Publishers: Dordrecht, Netherlands.

Sturm M, Perovich DK, Holmgren J. 2002. Thermal conductivity and heat transfer through the snow on the ice of the Beaufort Sea. *J. Geophys. Res. Oceans* **107**: 8043, doi: 10.1029/2000JC000409.

Sun X, Barros AP. 2014. High resolution simulation of tropical storm Ivan (2004) in the Southern Appalachians: Role of planetary boundary-layer schemes and cumulus parametrization. *Q. J. R. Meteorol. Soc.* **140**: 1847–1865, doi: 10.1002/qj.2255.

Svensson G, Holtslag AAM. 2009. Analysis of model results for the turning of the wind and related momentum fluxes in the stable boundary layer. *Boundary-Layer Meteorol.* **132**: 261–277, doi: 10.1007/s10546-009-9395-1.

Svensson G, Karlsson J. 2011. On the Arctic wintertime climate in global climate models. *J. Clim.* **24**: 5757–5771, doi: 10.1175/2011JCLI4012.1.

Tastula EM, Vihma T. 2011. WRF model experiments on the Antarctic atmosphere in winter. *Mon. Weather Rev.* **139**: 1279–1291, doi: 10.1175/2010MWR3478.1.

Tastula EM, Galperin B, Dudhia J, LeMone MA, Sukoriansky S, Vihma T. 2015. Methodical assessment of the differences between the QNSE and MYJ PBL scheme for stable conditions. *Q. J. R. Meteorol. Soc.* **141**: 2077–2089, doi: 10.1002/qj.2503.

Tjernström M, Leck C, Birch CE, Bottenheim JW, Brooks BJ, Brooks IM, Bäcklin L, Chang RY-W, de Leeuw G, Di Liberto L, de la Rosa S, Granath E, Graus M, Hansel A, Heintzenberg J, Held A, Hind A, Johnston P, Knulst J, Martin M, Matrai PA, Mauritsen T, Müller M, Norris SJ, Orellana MV, Orsini DA, Paatero J, Persson POG, Gao Q, Rauschenberg C, Ristovski Z, Sedlar J, Shupe MD, Sierau B, Sirevaag A, Sjogren S, Stetzer O, Swietlicki E, Szczodrak M, Vaattovaara P, Wahlberg N, Westberg M, Wheeler CR. 2014. The Arctic Summer Cloud Ocean Study (ASCOS): Overview and experimental design. *Atmos. Chem. Phys.* **14**: 2823–2869, doi: 10.5194/acp-14-2823-2014.

Tolk LF, Meesters AGCA, Dolman AJ, Peters W. 2008. Modelling representation errors of atmospheric CO_2 mixing ratios at a regional scale. *Atmos. Chem. Phys.* **8**: 6587–6596, doi: 10.5194/acp-8-6587-2008.

Town MS, Waddington ED, Walden VP, Warren SG. 2008. Temperatures, heating rates and vapour pressures in near-surface snow at the South Pole. *J. Glaciol.* **54**: 487–498, doi: 10.3189/002214308785837075.

van Ulden AP, Holtslag AAM. 1985. Estimation of atmospheric boundary layer parameters for diffusion applications. *J. Clim. Appl. Meteorol.* **24**: 1196–1207, doi: 10.1175/1520-0450(1985)024<1196:EOABLP>2.0.CO;2.

Van de Wiel BJH, Ronda RJ, Moene AF, De Bruin HAR, Holtslag AAM. 2002. Intermittent turbulence and oscillations in the stable boundary layer over land. Part I: A bulk model. *J. Atmos. Sci.* **59**: 942–958, doi: 10.1175/1520-0469(2002)059<0942:ITAOIT>2.0.CO;2.

Van de Wiel BJH, Moene AF, Jonker HJJ, Baas P, Basu S, Donda JMM, Sun J, Holtslag AAM. 2012. The minimum wind speed for sustainable turbulence in the nocturnal boundary layer. *J. Atmos. Sci.* **69**: 3116–3127, doi: 10.1175/JAS-D-12-0107.1.

Vickers D, Göckede M, Law BE. 2010. Uncertainty estimates for 1 h averaged turbulence fluxes of carbon dioxide, latent heat and sensible heat. *Tellus* **62B**: 87–99, doi: 10.1111/j.1600-0889.2009.00449.x.

Vihma T, Johansson MM, Launiainen J. 2009. Radiative and turbulent surface heat fluxes over sea ice in the western Weddell Sea in early summer. *J. Geophys. Res.* **114**: C04019, doi: 10.1029/2008JC004995.

Vogelezang DHP, Holtslag AAM. 1996. Evaluation and model impacts of alternative boundary-layer height formulations. *Boundary-Layer Meteorol.* **81**: 245–269, doi: 10.1007/BF02430331.

Westermann S, Lers J, Langer M, Piel K, Boike J. 2009. The annual surface energy budget of a high-Arctic permafrost site on Svalbard, Norway. *Cryosphere* **3**: 245–263, doi: 10.5194/tc-3-245-2009.

Wild M, Ohmura A, Gilgen H, Morcrette J-J, Slingo A. 2001. Evaluation of downward longwave radiation in general circulation models. *J. Clim.* **14**: 3227–3239, doi: 10.1175/1520-0442(2001)014<3227:EODLRI>2.0.CO;2.

Williams AG, Chambers S, Griffiths A. 2013. Bulk mixing and decoupling of the nocturnal stable boundary layer characterized using a ubiquitous natural tracer. *Boundary-Layer Meteorol.* **149**: 381–402, doi: 10.1007/s10546-013-9849-3.

Zhang T, Stamnes K, Bowling SA. 2001. Impact of the atmospheric thickness on the atmospheric downwelling longwave radiation and snowmelt under clear-sky conditions in the Arctic and Subarctic. *J. Clim.* **14**: 920–939, doi: 10.1175/1520-0442(2001)014<0920:IOTATO>2.0.CO;2.